OPTIMIZATION OF RECONSTRUCTION PARAMETERS IN BRAIN ACTIVATION STUDIES

by

ASWINI KANNEGANTI

Presented to the Faculty of the Graduate School of

The University of Texas at Arlington in Partial Fulfillment

of the Requirements

for the Degree of

MASTER OF SCIENCE IN BIOENGINEERING

THE UNIVERSITY OF TEXAS AT ARLINGTON

December 2008

ACKNOWLEDGEMENTS

I would like to thank all people who have helped and inspired me during my master's study and gave me the possibility to complete this thesis.

I especially want to thank my advisor, Dr. George Alexandrakis, for his guidance during my research and study at University of Texas at Arlington. His perpetual energy, stimulating suggestions and enthusiasm in research had motivated all his students, including me. In addition, he was always accessible and willing to help me with my endless questions and point me in the right direction when I got lost. As a result, research life became smooth and rewarding for me. I am grateful to Dr. Hanli Liu, my co-advisor for her unwavering support and help. Her knowledge on the practical aspects of optical imaging broadened my perspective and paved the way to better understanding of my thesis topic. Dr. Mario Romero-Ortega deserves special thanks as my thesis committee member and for encouraging me through the dissertation process and never accepting less than my best efforts.

I am indebted to friends, Nirupama, Kishan, Divya, Chaitanya and Himaja for their patient assistance regardless of the matter. My deepest gratitude goes to my father Sesha Sai, my mother Jayavani and my brother Anvesh, for their unflagging love and support throughout my life; this dissertation is simply impossible without them. To them I dedicate this thesis.

November 24, 2008

ABSTRACT

OPTIMIZATION OF RECONSTRUCTION PARAMETERS

IN BRAIN ACTIVATION STUDIES

Aswini Kanneganti, M.S.

The University of Texas at Arlington, 2008

Supervising Professor: George Alexandrakis

Diffuse Optical Imaging (DOI) is being extensively used in brain activation studies for the quantification of hemodynamic changes in the cerebral cortex. Many investigators have utilized the commercially available CW5 DOI device to attain cortical activation maps. However, the localization and spatial resolution in the resulting activation images remains poor. These limitations arise due to the large source detector separations required for light to reach the brain's surface and the limited number of detector channels in the CW5 system, which result in sparse spatial sampling of the cortical activation regions. In this thesis we assess the feasibility of using denser optode geometries to improve the localization and spatial resolution of activation regions for the existing CW5 system. The CW5 response to brain activity is simulated using Monte Carlo for different sizes, locations of activation regions and optode arrangements. It was found that maximizing the number of detector channels that can be accommodated by the CW5 system results in an improvement in spatial resolution of about 20%. As it is not possible to know the exact optical properties of the brain tissue structures, we also investigated the possibility that spatial resolution of the reconstructed images is compromised by incorrect assumption of these background optical optical properties. It was found that the improved

spatial resolution was robust to incorrect knowledge of the background tissue optical properties within their known physiological range of values. We conclude from these findings that the proposed detector geometries could improve image quality.

TABLE OF CONTENTS

LIST OF ILLUSTRATIONS

LIST OF TABLES

CHAPTER 1

INTRODUCTION

Neuronal activity is known to be correlated with arterial changes in local cerebral blood flow (CBF), local cerebral blood volume (CBV) and venous changes in the concentrations of oxyhemoglobin and deoxyhemoglobin. Collectively, these changes are referred to as “cerebral hemodynamics.” Oxyhemoglobin and deoxyhemoglobin absorb different wavelengths of light differently and thus their concentrations could be calculated through measurements made at different wavelengths. Near-Infrared light is weakly absorbed by the skull and the absorption differences for oxyhemoglobin and deoxyhemoglobin are also observed in this region and hence it can be used to gauge the brain activity beneath the skull. A variety of techniques can be used to detect these changes. Diffuse Optical Imaging (DOI) is unique in that it is a non-invasive and portable technique.[1]

1.1 Diffuse Optical Imaging

In a typical DOI system, light is applied into tissue and is then detected near points on the tissue surface. The light used for imaging should penetrate deeper in order to reach cortical tissue located centimeters below the surface. As an approximate rule of thumb for frequency domain and continuous wave measurements--the depth of maximum brain sensitivity is approximately half the source-detector separation distance [26]. A spectral window exists within tissues in the near-infrared (NIR) from approximately 700 nm to 900 nm, wherein photon transport is dominated by scattering rather than absorption. Increased scattering means that the photons traverse through tissues via diffusion transport. The DOI measures the change in the detected signal which corresponds to Near-Infrared light absorption for ‘before activation’ and ‘after activation’ due to the accumulation of blood in the cortical activation region. The characteristic absorption spectra for oxyhemoglonin and deoxyhemoglobin in the near infrared region of the electromagnetic spectrum is shown in the figure 1.1.

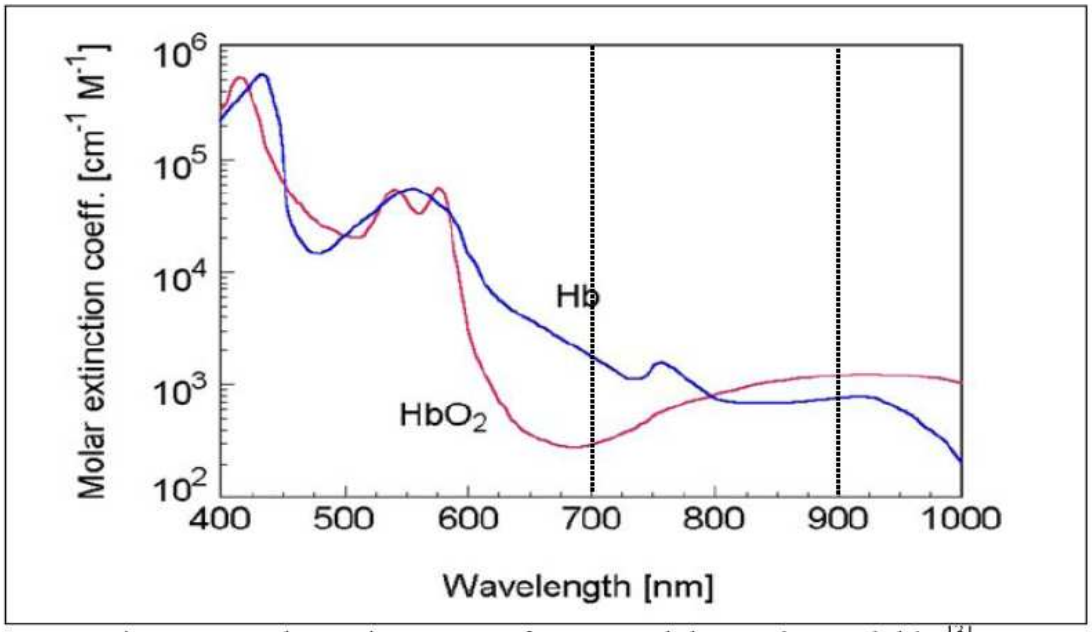

Figure -1.1: Absorption spectra for oxy and deoxy - hemoglobin

The absorption of hemoglobin and water is small in the near-infrared, but elastic scattering from organelles and other microscopic interfaces is large. These are the conditions required for application of the diffusion model for light transport. For many biological tissues, the absorption length for NIR light is much longer than the scattering length**.** Using the diffusion model it is possible to quantitatively separate the effects of tissue scattering from tissue absorption, and to accurately incorporate the influence of boundaries, such as the air-tissue interface, into the light transport theory. The diffusion approximation also provides a tractable basis for tomographic approaches to image reconstruction using highly scattered light [2]. Three measurement schemes are used for these evaluations: Time Domain, Frequency Domain, and Continuous Wave (CW). Measurements are made in transmission, reflection, or both. Of these three measurement types, the CW method is the simplest, least expensive, and provides the fastest data collection [3].

1.2 Continuous Wave (CW) Near-Infrared Reflectance Systems

Continuous Wave (CW) systems require a light source that either emits at a constant intensity, or is modulated at a low (1-10 kHz) frequency in order to eliminate background noise and multiplies signal detection.

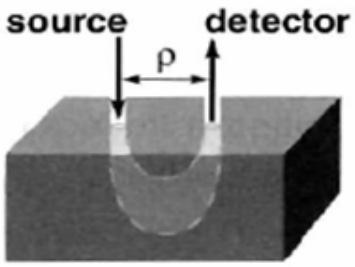

Figure -1.2: CW Measurement setup

Figure 1.2 shows the experimental setup for CW measurement. The light pathway inside the tissue varies with source – detector separation. The sensitivity region inside the tissue is banana shaped and extends approximately half the source detector separation. Probably the most highly developed application of CW imaging technology is the study of haemodynamic and oxygenation changes in superficial tissues, and of the outer (cortical) regions of the brain in particular using DOI [27]. This typically involves acquiring multiple measurements of diffuse reflectance at small source–detector separations over the entire activation area of tissue simultaneously. The reflectance measurements are in turn used to form the reconstruct images of the imaged tissue. These images may display the specific absorption and scattering properties of the tissue, or physiological parameters such as blood volume and oxygenation, or oxy- & deoxy- hemoglobin concentrations [4].

Functional optical brain imaging techniques require a faster data acquisition rate for filtering undesired hemoglobin changes arising from various physiological factors like cardiac

pulses, respiratory effects and cerebral vasomotion. It is also necessary to cover the full spatial extent of the activation areas that typically span the brain; such spatial coverage is not limited to the activation area but extended to the areas that are not involved with the stimulation. This helps in getting contrast between regions of activation and surrounding. The Optical Imager CW5 (TechEn Inc., Milford, MA) (See Section 2.1) satisfy the above requirements; hence can be used for functional brain imaging. CW5 uses HoMER (See Section 2.2), data analysis software for optical reconstruction of the reflectance data.

1.3 The Need for Improvement in the Spatial Resolution of the CW5 System

Though the existing CW5 gives important results for the brain activation studies, there is scope for the improvement in localization of the activation region and the spatial resolution. Reflection geometry used for measuring brain activation in humans requires >3cm source detector separation for attaining the penetration depth to record signals from the cortex which is ~2cm below the head surface as calculated from the brain anatomical scan images. The existing optode geometry for CW5 system uses 8 channels for sources and another 8 for detectors for scanning one cerebral hemisphere. The images are reconstructed by computing the change in the absorption coefficients due to activation from the reflectance data detected on the surface of the tissue and is termed as the inverse problem. The exact solution to the inverse problem does not exist due the fact that more number of unknowns exist than the number of measurements done. The optimal solution of the inverse problem compromises the quantitative accuracy. As the CW5 system has provision to include a maximum of 12 channels, the possibility of improving the quality of the reconstructed images in terms of improved spatial resolution and activation localization can to be addressed. By opting for denser optode geometries we can increase not only the spatial sampling of the imaging volume but also increase the number of measurements. The location of the activation region relative to the optode arrangement and the source detector separation affects the spatial resolution. Thus

effective positioning of the available channels can also affect the quality of the reconstructed images.

1.4 Prior Work in the Field

1.4.1 Improving the diffuse optical imaging spatial resolution of the cerebral hemodynamic response to brain activation in humans

In a recent paper published by the Photon Migration Labs[25][6], investigation was done on different probe geometries and it concluded that a hexagonal geometry is the best available option because of current technology limitations which include the limited dynamic range fro the detectors, size of detectors and sources. The geometries were set with the longer source detector separation to 4.25 cm, which resulted in a shorter separation of 2.5 cm when the nearest neighbor measurements are also taken into account. The absorption imaging matrix A was calculated using the Rytov approximation for a semi-infinite medium with μ_s '= 10 cm^{-1} and μ_a = 0.1 cm^{-1}. The sources and detectors were placed on the planar surface of the tissue mimicking phantom, and the absorption image was constrained to a plane at a depth of 1.5 to 2.0 cm below the surface. The vector of measurements y is given by y = A x where the ith element of x corresponds to the absorption change in the ith voxel in the plane at a depth of 1.5 to 2.0 cm.

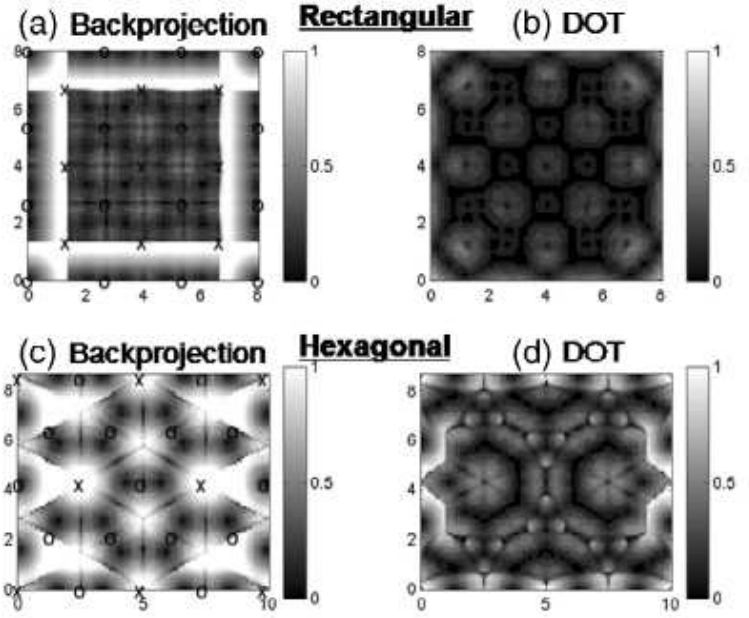

Figure-1.3: Localization error for (a), (b) the rectangular and (c), (d) the hexagonal geometries compared for (a), (c) backprojection and (b), (d) DOT image reconstructions.The sources (crosses) and detectors (open circles) are shown in (a) and (c) The scale goes to 1 cm, where white indicates greater than 1-cm localization error [25]

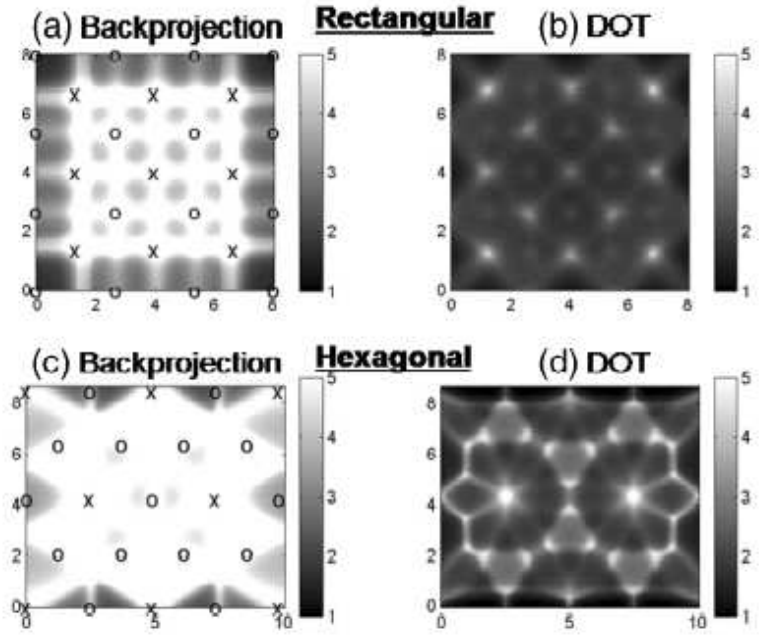

Figure-1.4: Resolution for (a), (b) rectangular and (c), (d) hexagonal geometries compared for (a), (c) backprojection and (b), (d) DOT image reconstructions. The sources (crosses) and detectors (open circles) are shown in (a) and (c). The scale ranges from 1 to 5 cm^2, where white indicates greater than 5 cm^2 [25]

It was shown that incorporating second nearest- neighbor measurements into a diffuse optical image reconstruction of brain activation significantly improves image resolution and localization accuracy by a factor of 2 compared with back projection imaging with only nearest-neighbor measurements. The work compared rectangular and hexagonal geometries of sources and detectors and found that, whereas the rectangular geometry is slightly better, it is easier to implement the hexagonal geometry experimentally because the hexagonal geometry requires less switching between subsets of sources, has a greater measurement duty cycle, and requires a smaller dynamic range. It was then experimentally demonstrated that there is significant improvement in image resolution afforded by a human brain function imaging experiment with the hexagonal geometry [25] [6].

1.4.2 Improving performance of reflectance diffuse optical imaging using a multicentered mode

In the paper published by the Chinese academy of sciences [22], a novel multicentered mode for arrangement of optical fibers to improve the imaging performance of reflectance diffuse optical imaging was proposed. Simulations performed using a semi-infinite model show that the proposed multicentered geometries can achieve a maximum of 42 overlapping measurements. The contrast to noise ratio analysis indicates that the best spatial resolution is 1 mm in radius and the contrast resolution is less than 1.05 for the multicentered geometries. The results from simulations indicate significant improvement in image quality compared to the singlecentered mode and previous geometries. Additional experimental results on a single human subject lead to the conclusion that the proposed multicentered geometries are appropriate for exploring activations in the human brain. In the case of single density geometries, there are 12 detectors and for double density there are 24 detectors. Similarly, for single centered geometries only one source is used and for multicentered geometries, 6 sources are utilized [22].

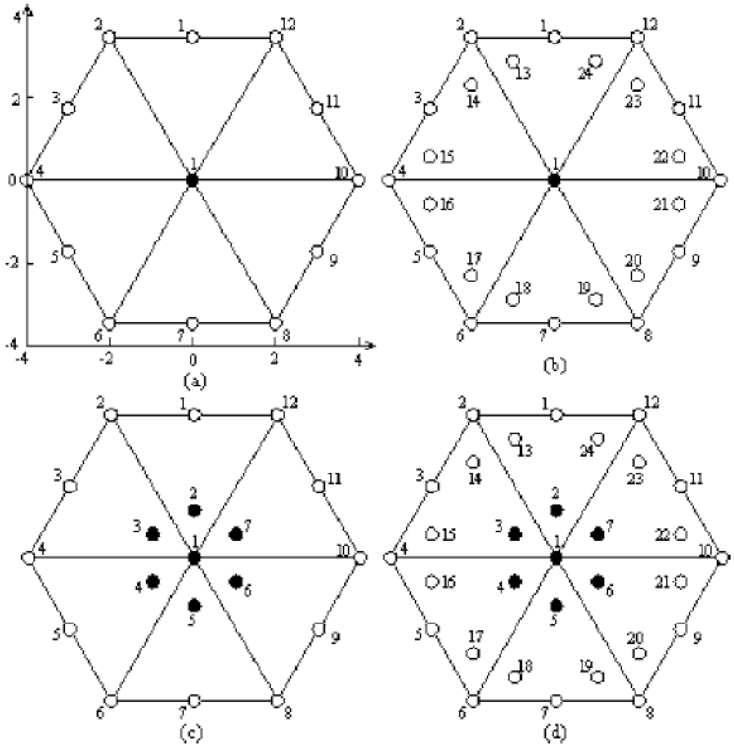

Figure-1.5: (a) Single-centered single-density (SS) geometry, (b) single-centered double-density (SD) geometry, (c) multicentered single-density (MS) geometry, and (d) multicentered double-density (MD) geometry. The sources and detectors are indicated by dots and open circles, respectively [22]

The measurements achieved in the four geometries were SS - 12, SD - 24, MS - 84, and MD - 168. The imaging regions of the four geometries were the regions covered by the hexagons, and the pixel sizes were 1X1 mm. A semi-infinite model with an absorption coefficient of 0.1 cm−1 and a reduced scattering coefficient of 10 cm−1 was used in the simulations. The sources and detectors were placed on the air/tissue surface in the model, and the forward matrix ***A*** was calculated by the Rytov approximation. Absorbers were located in the model [22].

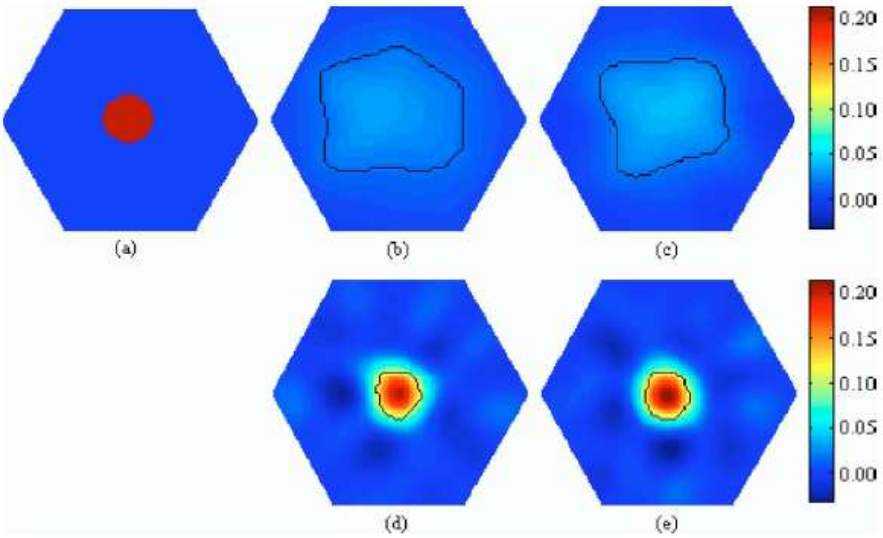

Figure-1.6: The (a) true image and the reconstructed images using (b) SS, (c) SD, (d) MS, and (e) MD geometries in position 1. The objects were located 1.5 cm deep in a semi-infinite model. The black lines indicate the objects detected using the half-maximum method[22]

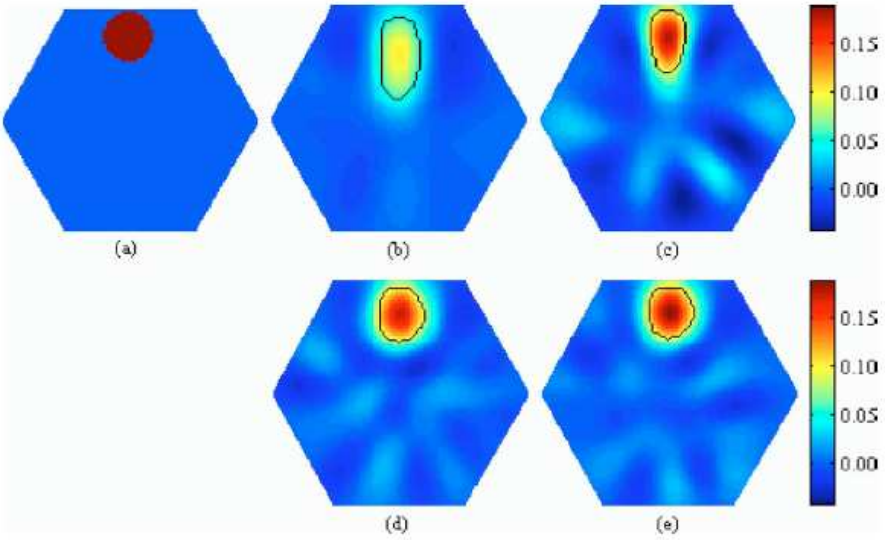

Figure-1.7: The (a) true image and the reconstructed images with the (b) SS, (c) SD, (d) MS, and (e) MD geometries in position 2. The objects were located 1.5 cm deep in a semi-infinite model. The black lines indicate the objects detected using the half-maximum method[22]

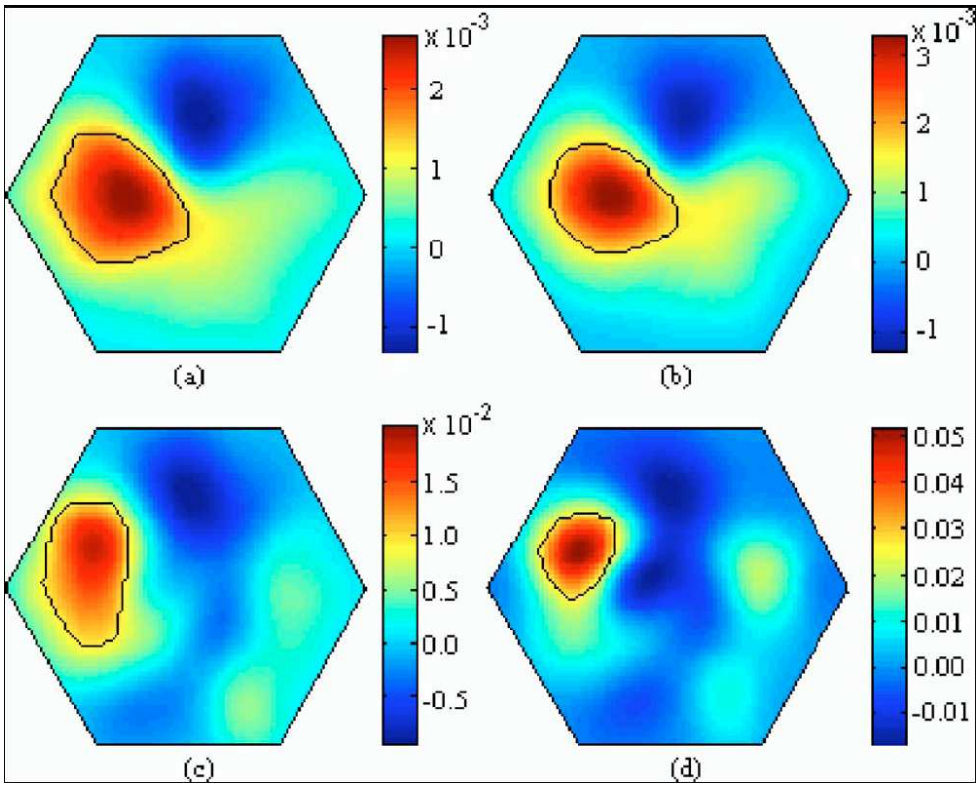

Figure-1.8: Reconstructed images using the (a) SS, (b) SD, (c) MS, and (d) MD geometries from the experiments on a human subject[22]

The results from the simulations show a significant enhancement in image quality compared with both single-centered and previous geometries. The multiseparations in the multicentered geometries are helpful for improving depth resolution [22].

1.5 Thesis Goals

The previously published work [12] [23] [22] discussed above indicates that spatial resolution and localization accuracy could be enhanced by increasing the number of source-detector pairs involved in a measurement. In those studies the maximum number of source and detector channels available on the CW5 system, namely 32, were used to attain the highest possible spatial sampling in reflectance measurements and as a result attain the highest possible spatial resolution. However, the current state of our CW5 system accommodates only 24 source (12 at 690 nm and 12 at 830 nm) and 24 detector channels. In the current setup the

jackets of source and detector optical fiber bundles each extend over an area of 1x2 cm. The number of sources and detectors that can therefore be fit on the scalp's surface without running into each other is limited. *The purpose of this work is to attain cortical activation maps for both oxy- and deoxyhemoglobin, over both brain hemispheres, at the highest practically possible detector spatial sampling that can be attained with our CW5 system.* More specifically, we have assessed the effect of different source and detector arrangements on the spatial resolution of cortical activation maps for different activation region sizes, locations, contrast and of errors in the assumed background optical properties. In addition, the regularization parameter of the reconstructions, which controls the balance between noise and spatial resolution in an image, was optimized using the L-curve method [21].

CHAPTER 2

METHODS AND MATERIALS

2.1 Overview of CW5

CW5 is designed to perform multi-wavelength, continuous wave, near infrared, diffuse optical tomographic measurements at very high sampling rates (Fig. 2.1). CW5 system uses frequency-division multiplexed laser sources.

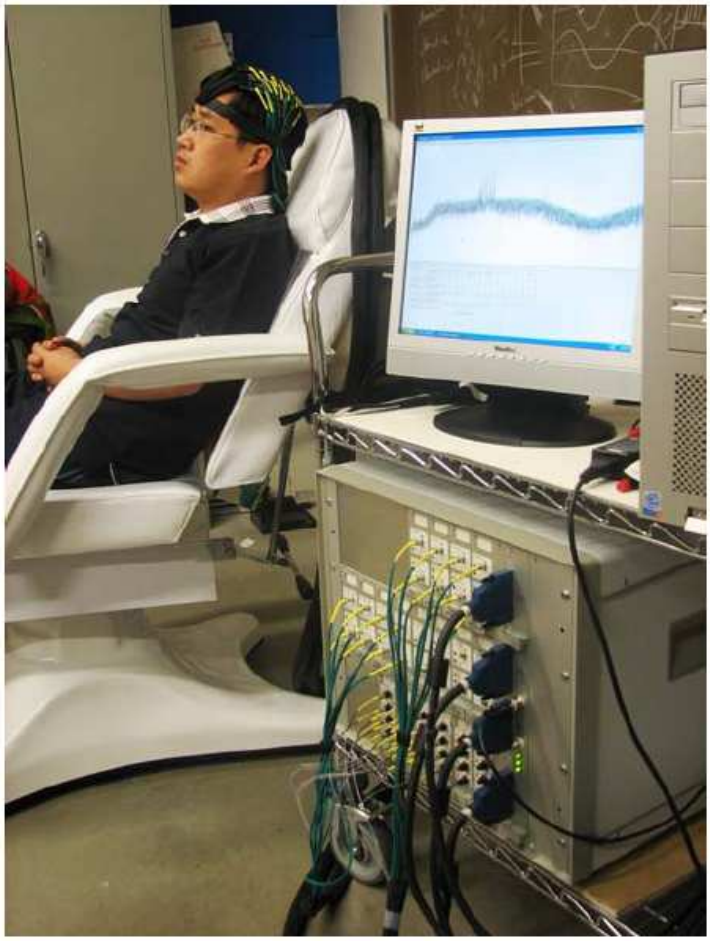

Figure-2.1: CW5 System

The lasers are at two source wavelengths, 690 nm and 830 nm, and split evenly between 24 sources (i.e.12 lasers at each wavelength). The odd numbered lasers function at 690 nm and the even numbered ones at 830 nm. The measured power at the output of 690 nm sources is adjusted to emit near 9 mW and the 830 nm sources near 5 mW. Lasers are square-wave modulated at a frequency band ranging from 6.4 kHz to 11 kHz, with an interval of 200 Hz between adjacent frequencies. “Continuous parallel operation of all the sources and detectors has been demonstrated to allow rapid data collection.”[7][8]

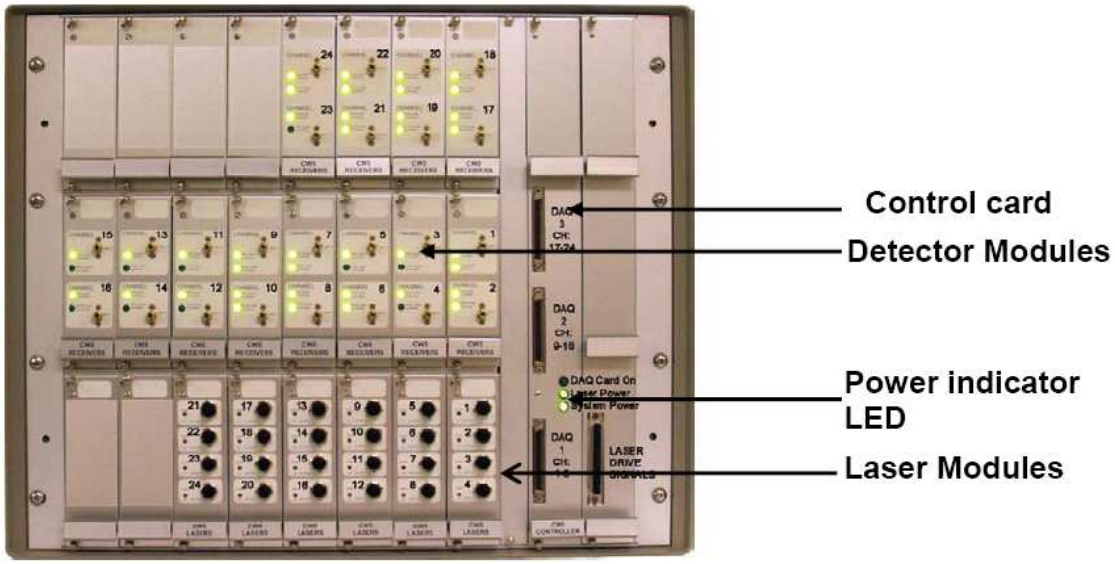

Figure- 2.2: Front Panel Of CW5 [7]

The CW5 instrument has 24 transmitter channels (lasers sources) and 24 receiver channels (detectors) and has provision to increase the number to 32 channels. The unit houses 21 cards: 6 transmitter cards with the four lasers each, 12 receiver cards with two detectors each, one control card with 3 connectors to National Instrument data acquisition cards, and one clock buffer card. Figure-2.2 above shows the locations of the twenty-one cards looking at the front panel of the instrument.[7]

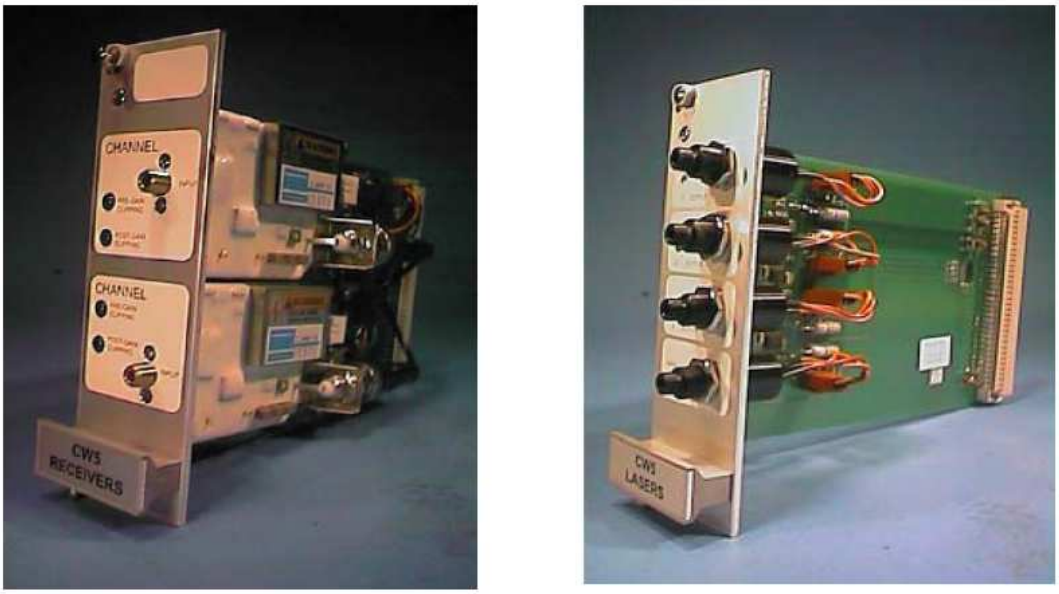

Figure -2.3: Transmitter card (left) and Receiver card (right)[7]

Figure-2.3 shows laser source transmitter card and receiver card for the system. Each laser source card has four sources, 2 of each wavelength. The system has 6 such cards arranged in parallel on the front panel, giving 12 sources of each wavelength. Each receiver card has two APD detectors, 12 such cards are present on the system making the total number of detectors to 24. The 24 receiver channels generate a set of 24 single ended analog signals. The controller (shown in figure-2.2) buffers and converts these 24 single ended signals to 24 differential pairs and drives them out the analog signal connector [7].

2.2 Data Processing Environment

*HomER (**H**em**o**dyna**m**ic **E**voked **R**esponse)* is a graphical user interface developed to analyze the functional Near-Infrared Spectroscopy (NIRS) data. It has tools for filtering, data averaging, linear regression, and 2D image reconstruction. “HomER is designed to work with NIRS data from most source and experimental set-ups, allowing the user full control of the measurement configuration and probe properties [8].

HomER can be divided in to 4 sub sections: Section-1: Signal Processing, Section-2: Response Processing, Section-3: Image Reconstruction, Section-4: Region of Interest Analysis.

Section-1: Signal processing

This section of HomER incorporates windows displaying raw data and probe geometry. It contains tools for filtering time-courses with band-pass filters and principal component analysis (Fig. 2.4). PCA helps in removal of systemic fluctuation and artifact.[9]

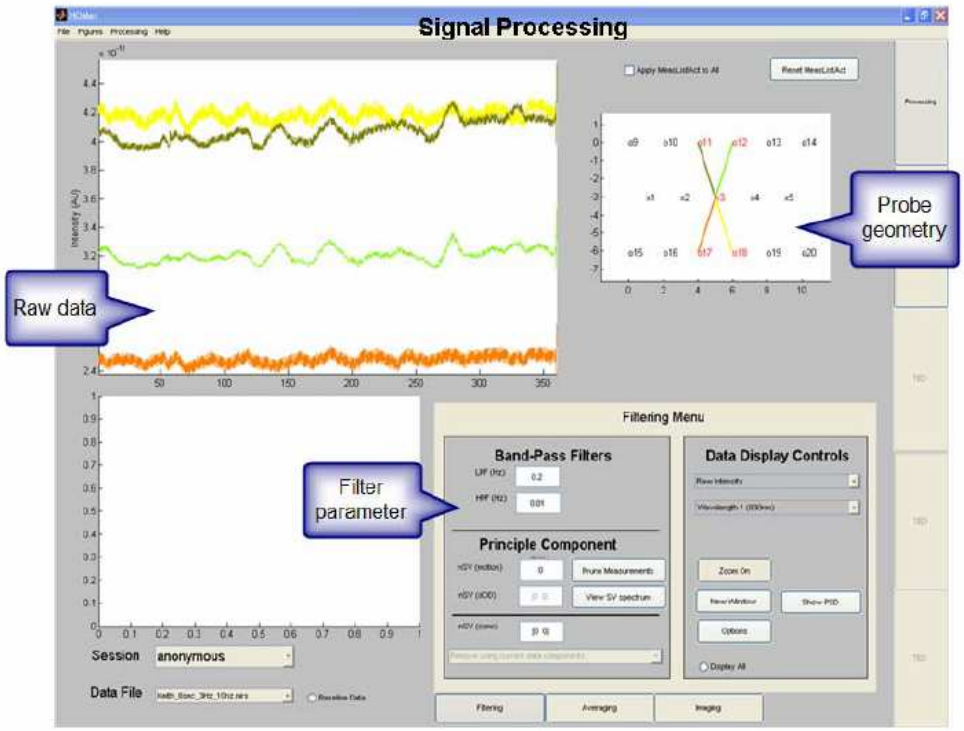

Figure-2.4: Signal Processing section of HomER

Section-2: Response Processing

This section of HomER is dedicated for analyzing functional hemodynamic responses (Fig. 2.5). In addition to multiple condition experimental designs, this also supports block-designed and event-related paradigms. The hemodynamic response curves are displayed as per their respective optode location, which helps in localization of activity. Responses can be analyzed for entire experimental run or can be averaged over blocks of time interval. The parameters for block averaging and stimulus markers can be adjusted with the help of GUI in

this section. Individual channels or blocks of time-points can be selected to be disregarded in analysis, helping in rejection of motion or other artifacts.[9]

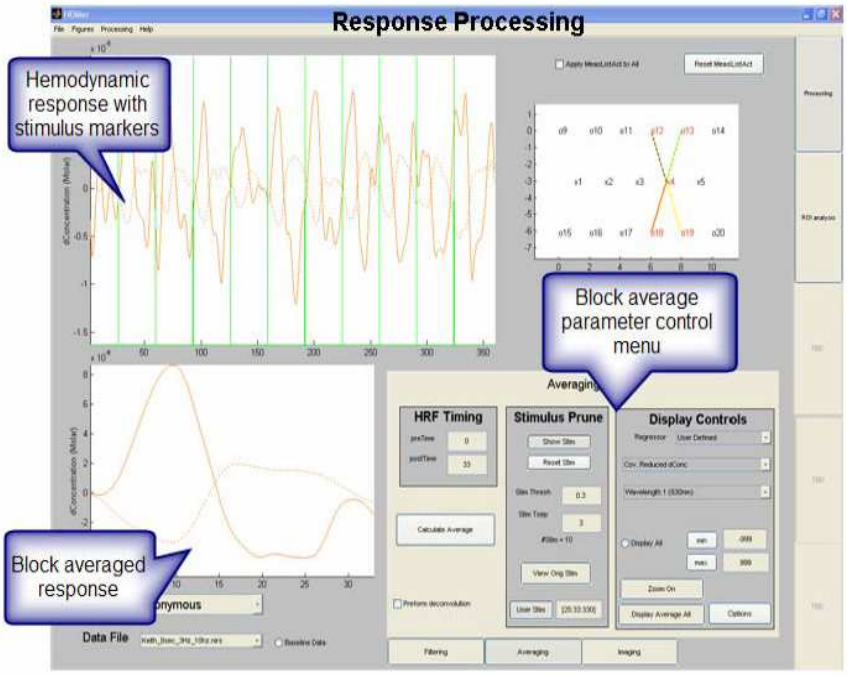

Figure-2.5: Response processing section of HomER

Section-3: Image Reconstruction

HomER offers various options for basic image reconstruction including backprojection and other regularized inversion techniques. This section is capable of reconstructing both optical density and hemoglobin concentration images. The response time for reconstruction can be varied with the help of Slide bar, allowing better control over image reconstruction. The imaging parameter control menu provides the options for varying the absorption and scattering coefficients, the voxel sizes and reconstruction depths (Fig. 2.6).

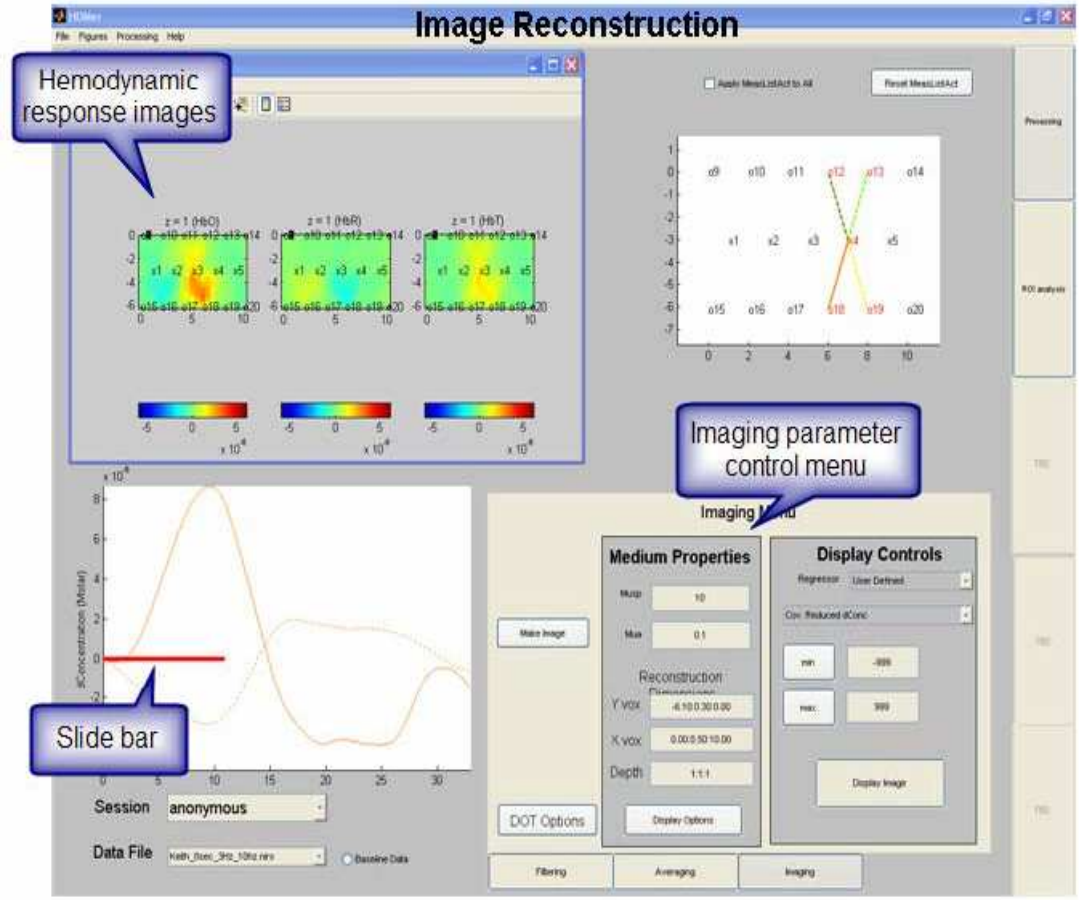

Figure-2.6: Image Reconstruction section of HomER

Section-4: Region of Interest Analysis

Section-4 of HomER has the capability of performing Region-of-Interest (ROI) analysis. ROI averages can be calculated for individual subjects or group of subjects and across multiple sessions. The regions of interest can be defined by source-detector channel or within the reconstructed image. It calculates the Hemodynamic Response Function (HRF) for the selected region (Fig. 2.7). Comparison between response functions of various subjects can be done in this section.

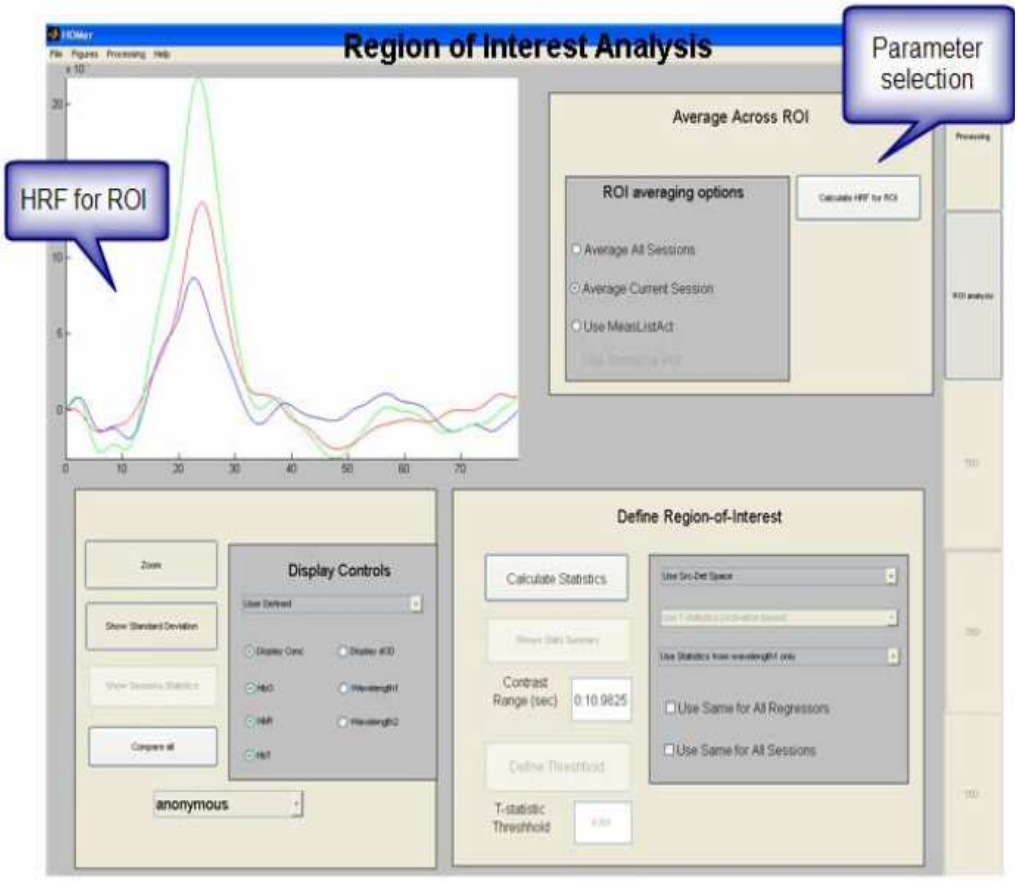

Figure-2.7: Region of interest analysis section of HomER

2.3 Monte Carlo Simulations

The tMCimg Monte Carlo Transport Program uses a Monte Carlo algorithm to model the transport of photons through 3D volumes with spatially varying optical properties and arbitrary boundary conditions. Both highly scattering tissues and weakly scattering tissues are supported. The simulation begins by launching a photon into the tissue.

Step 1: The initial position and direction are set according to the configuration file. The photon propagates with small, fixed incremental step sizes.

Step 2: The fixed stepsize Δs must be small relative to the average mean free path length of the photon in the tissue.

$\Delta s << 1/\mu_t = 1/ (\mu s + \mu_{a)}$

Where μ_t , μs and μ_a are the total attenuation, the absorption, and the scattering coefficients respectively.[10]. The step size is an exponentially distributed random variable.

Step 3: The photon is moved to the next scattering event undergoing internal reflection, refraction at surfaces and absorption. As it moves from voxel to voxel, it is attenuated to the local absorption and the distance traveled in each tissue type is recorded.

Step 4: As the photon moves, its position is sampled at regular time intervals and this is used to update the accumulated photon density.

Step 5: Scatter into a new direction according to some phase function.

Step 6: Iterate until the photon leaves the system, or the time limit is exceeded.

Step 7: If the photon exists near a detector, add a line to the history file. Final photon density is saved. The fluence or the integrated flux at the detector is computed by adding the detected photons and by scaling to the location.

2.4 The Semi - Infinite Medium Diffusion Solution

The radiative transport equation (RTE) describes the propagation of light in all media and can accurately model the directionality of the incident source and detectors at realistic source/detector separations. The RTE is a most accurate model for the migration of photons in general, but is typically difficult to solve without introducing approximations [11]. The diffusion approximation of RTE is typically used in it's place. The Diffusion equation is

$$\nabla \cdot D(\mathbf{r}) \nabla \Phi(\mathbf{r}, t) - v\mu_a(\mathbf{r})\Phi(\mathbf{r}, t) + vS(\mathbf{r}, t) = \frac{\partial \Phi(\mathbf{r}, t)}{\partial t}. \quad (1)$$

$\Phi(\mathbf{r}, t)$ is proportional to the photon number density $U(\mathbf{r}, t)$ (photons/cm^3), that is, $\Phi(\mathbf{r}, t) = vU(\mathbf{r}, t)$. The turbid medium is characterized by a speed of light, v, an absorption coefficient μ_a (i.e., the multiplicative inverse of the photon absorption length), and a photon diffusion coefficient, $D = v/3(\mu'_s + \mu_a) \cong v/3(\mu'_s)$; since in most tissues $\mu'_s \gg \mu_a$. The medium's reduced scattering coefficient is defined as $\mu'_s = (1 - g)\mu_s$ and represents the multiplicative inverse of the photon random walk step length, l^*. Here, μ_s is the reciprocal of the photon scattering length, l, and g =

$<\cos\theta>$ is the ensemble-averaged cosine of the scattering angle θ associated with a typical single scattering event in the sample; g accounts for the fact that light is more typically scattered in the forward direction, so that many scattering events are required before the initial photon propagation direction is truly randomized. $S(\mathbf{r}, t)$ is an isotropic source term that provides the number of photons emitted at position $\mathbf{r}$ and time t per unit volume per unit time.[12]

Diffuse optical imaging measurements on the brain typically have source-detector separations of 2–4 cm; the head can be considered a semi-infinite medium locally. This simplistic assumption enables an analytic solution of the diffusion equation [12] [14] and to be used for simulations to test the accuracy and resolution of diffuse optical imaging experiments [15][16] .Such simplified simulations are valuable for guiding the optimization of experimental design, which can then be verified with more sophisticated simulations.

The absorption and scattering properties of the tissue are wavelength-dependent. The absorption coefficient of the medium is proportional to the concentration of the different chromophores within the medium. For near-infrared wavelengths of 650 to 950 nm, the dominant chromophores in tissue are oxy- and deoxyhemoglobin. Thus, the wavelength-dependent absorption coefficient is given by

$$\mu_a\lambda=\varepsilon_{HbO2}\lambda[HbO_2]+\varepsilon_{HbR}\lambda[Hbr] \qquad (2)$$

Where λ indicates the photon wavelength, $\varepsilon_{HbO2}(\lambda)$ and $\varepsilon_{HbR}(\lambda)$ are the intrinsic wavelength-dependent extinction coefficients of oxy- and deoxyhemoglobin, respectively, and $[HbO_2]$ and [HbR] are the local hemoglobin concentrations that can vary in space and time. Through spectroscopic measurements of the absorption coefficient, we can thus estimate the hemoglobin concentrations.

Generally, the change in detected intensity denoted as a change in optical density, ΔOD, is linearly proportional to a small change in the absorption coefficient

$$\Delta \mathrm{OD}(t,\lambda) = -\log\left(\frac{\Phi(t,\lambda)}{\Phi_0(\lambda)}\right) = \Delta\mu_a(t,\lambda)L(\lambda), \tag{3}$$

Where the logarithm is a natural logarithm, Φ_o is the average detected photon fluence, and L is the effective average path length of light through the tissue experiencing the absorption change [17] [18]. These parameters are wavelength-dependent. The effective path length is independent of time when the temporal absorption changes are small. This formulation is known as the modified Beer-Lambert law [18] [19].

The modified Beer-Lambert law can be generalized for a set of discrete volume elements (i.e., voxels), each having a potentially different absorption change.

$$\Delta \mathrm{OD}_i(t,\lambda) = \sum_{j=1}^{N_{vox}} \Delta\mu_{a,j}(t,\lambda)L_{i,j}(\lambda) \tag{4}$$

Where $L_{i,j}$ is the effective path length of detected photons for the ith measurement in the jth voxel. Eq. (4) can be written in matrix form as $\mathbf{y} = \mathbf{A}\cdot\mathbf{x}$ and can be derived from the photon diffusion equation [Eq. (1)] using the Rytov approximation [20], which finds

$$L_{i,j}=\Phi_0(r_{s,i},r_j)\Phi_0(r_j,r_{d,i}), \tag{5}$$

where $\mathbf{r}_{s,i}$ and $\mathbf{r}_{d,i}$ are the source and detector positions, respectively, for the ith measurement.

This is the basis of image reconstruction algorithms in which an image of $\Delta\mu_a$ (i.e., the vector $\boldsymbol{x}$) can be obtained from a set of measurements (i.e., the vector $\boldsymbol{y}$) through inversion of the matrix $\mathbf{A}$ (i.e., the effective pathlengths $L_{i,j}$).

For the usual case of fewer measurements than unknowns, the linear problem is underdetermined and is given by the regularized Moore-Penrose generalized inverse

$$\hat{\mathbf{x}} = \mathbf{A}^T\left(\mathbf{A}\mathbf{A}^T + \alpha s_{\max}\mathbf{I}\right)^{-1}\mathbf{y}, \tag{6}$$

where $\mathbf{I}$ is the identity matrix, s_{max} is the maximum eigenvalue of $\mathbf{A}\mathbf{A}^T$, and α is the regularization parameter.[12]

2.4.1 Regularization Parameter Selection

The value of optimized α is estimated from the L curve. The L-curve is a log-log plot of the norm of a regularized solution versus the norm of the corresponding residual norm. L curve can also be drawn between differentiated relative error and the alpha values. It is a convenient graphical tool for displaying the trade-off between the size of a regularized solution and its fit to the given data, as the regularization parameter varies. The L-curve thus gives insight into the regularizing properties of the underlying regularization method, and it is an aid in choosing an appropriate regularization parameter for the given data [21]. The L curve drawn for the Monte Carlo simulations and the diffusion solution resulted in α = 0.1, which is set for all results throughout this paper.

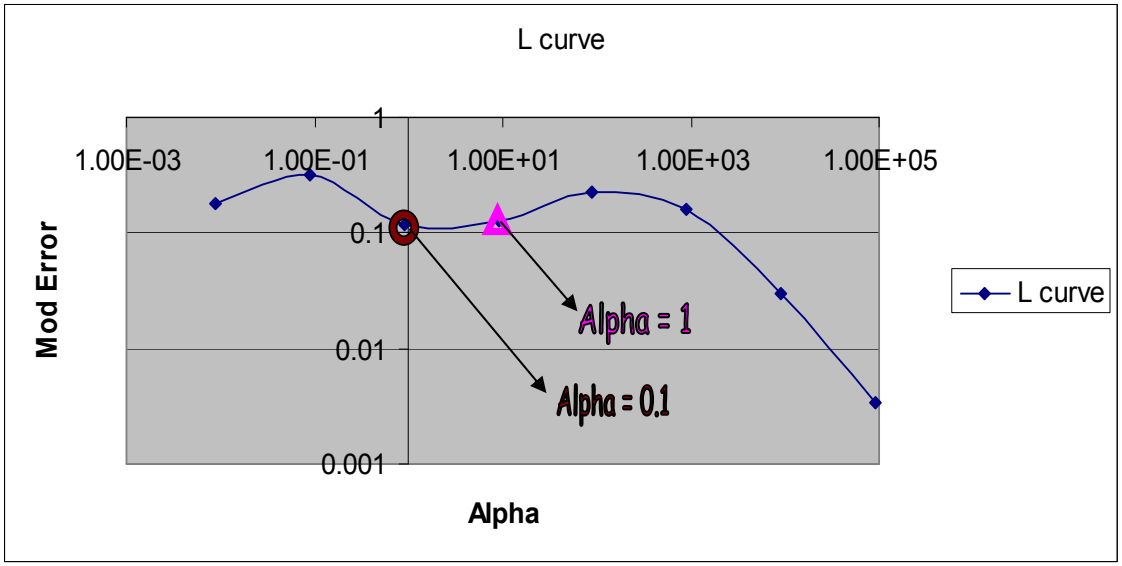

Figure-2.8: L curve plot between the differentiated α Vs Relative Error in Y

The Figure 2.8 shows the L curve plot, and it is seen form the plot that the maximum change in the curvature is observed during α equals 0.1 and 1 respectively. The reconstructed images obtained are shown in Figure 2.9.

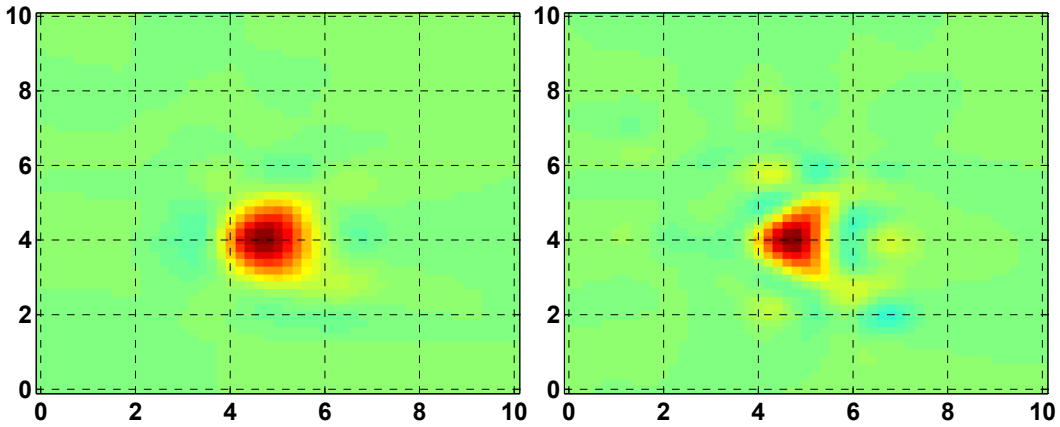

Figure-2.9: The reconstructed images obtained for activation region for α = 1(right) and α = 0.1(left)

Figure 2.9 shows the reconstructed images obtained with α =1 and α =0.1. It is observed that the point spread in the case of α =0.1 is better in contrast to α =1. Thus regularization parameter was chosen as 0.1 for the work done.

The diffusion solution based on the above equations is implemented in MATLAB. The A matrix is calculated using rytov approximation for the background optical properties and the calculated extrapolated boundary conditions. The change in the optical density is calculated from the reflectance data calculated by the Monte Carlo simulations for diverse activation regions using different optode geometries. The image is reconstructed using the Tikinov regularization inversion. The flow chart for the same is given in figure 2.10 and the actual code is in the Appendix 1.

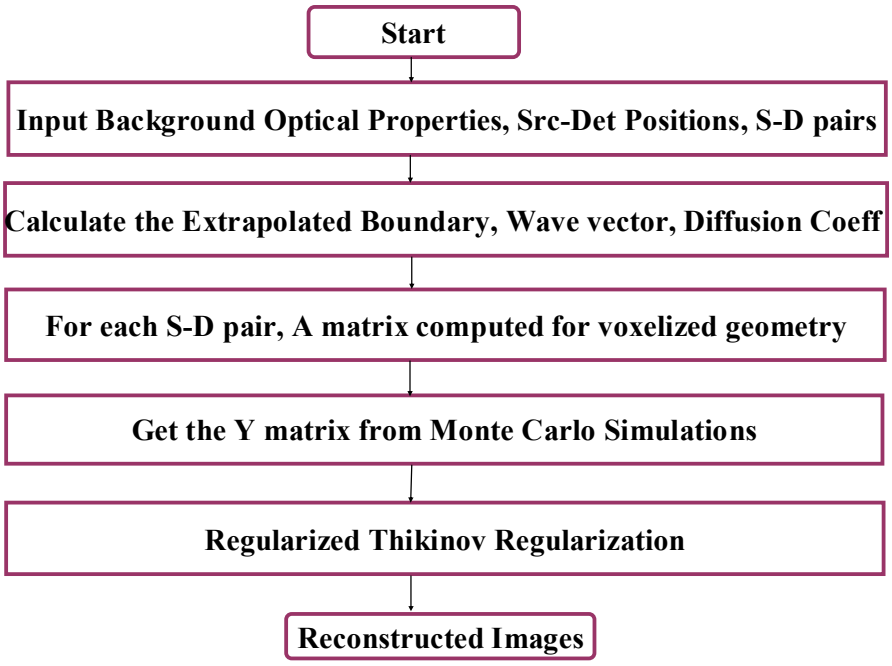

Figure-2.10: Flow chart of the reconstruction algorithm

2.5 Simulated Geometry

2.5.1 Optical Properties

The simulations are done at the wavelength of 690 nm which is typically used in CW5. The optical properties at this wavelength chosen are μ_a = 0.025 mm^{-1} and μ_s' = 1.05 mm^{-1}, which correspond to the typical brain white matter/gray matter properties. [22]

2.5.2 Anomaly Locations

The reflectance data was simulated for square anomalies of sides 0.6cm, 1cm and 2cm at depth of 0.5-1 cm. For the depth localization, simulations are done for square anomaly of side 2cm at depths 0.5-1cm, 1-1.5cm, 1.5-2cm and 2-2.5cm. The μ_a in the activated regions is perturbed by 80% and 40 % from the anomaly absorption coefficient for all the above cases.

2.6 Proposed Geometries

The existing CW5 instrument has a provision for 24 channels to cater to the sources and detectors electronics. The existing CW5 optode geometry for one hemisphere of the brain is shown in Fig 2.11.

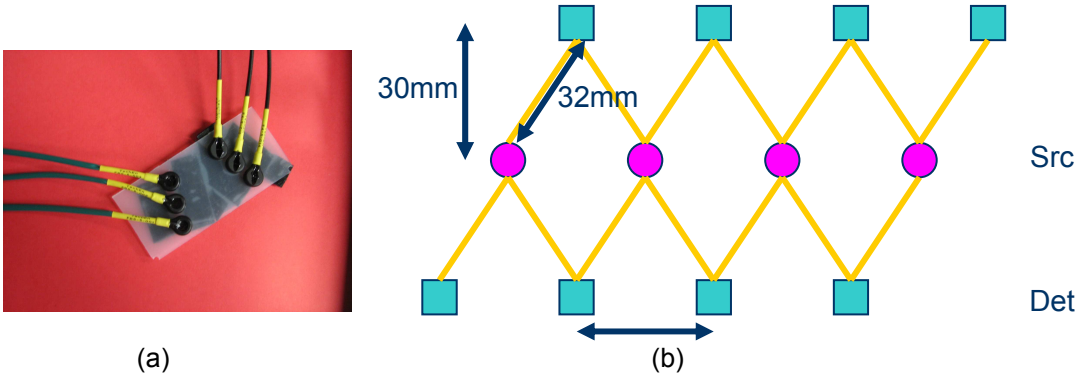

Figure -2.11: (b) CW5 Optode Geometry and (a) CW5 actual detector setup

The CW5 optode geometry is a rectangular geometry of 4 sources and 8 detectors spanning 8cm X 6cm with 14 measurements. It is seen from the above figure, that there is large source detector separation and the number of source detector pairs are small. Hence, in order to improve the quality of the reconstructed images, 4 optode geometries are proposed. The Diffuse Optical Imager has 12 channels for detectors per hemisphere as described earlier but for the optode geometry shown in Fig 2.11, only 8 channels are used. The remaining channels could cater to the addition of four more detectors to the existing geometry. The following 4 optode geometries shown in Figure 2.12 are proposed for the same. The Proposed Geometry (PG) IV is the geometry with the maximum possible detectors that can be added.

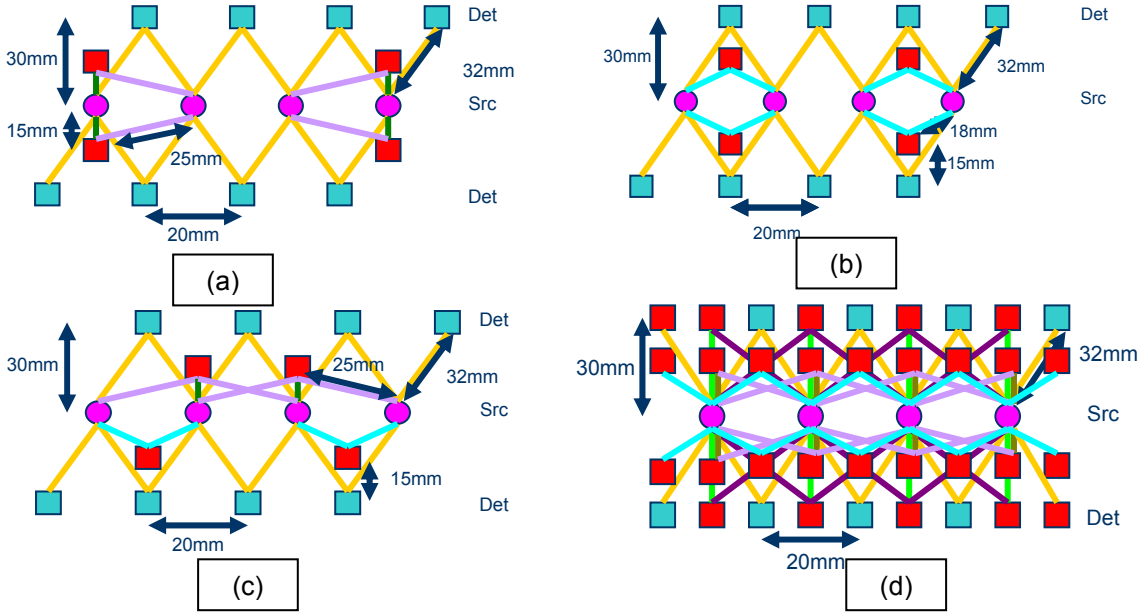

Figure-2.12: (a) Proposed Geometry (PG) I, (b) Proposed Geometry (PG) II, (c) Proposed Geometry (PG) III, (d) Proposed Geometry (PG) IV

The idea behind the proposed geometries is to increase the number of spatial sampling for the imaging volume. All the proposed geometries are rectangular in shape and cover 8cm X 6cm. In the PG I, PG II and PG III four detectors are added with source detector separations of 15mm, 18mm and 25mm respectively. In the PG IV, a total of 28 detectors are added forming 4 rows of detectors each at 15mm and 30mm away from the sources. The geometries produce a large number of measurements when the nearest and second nearest neighbor sources and detectors are considered. PG I and PG II has 22 measurements in total and PG III has 24 measurements and PG IV has the maximum with 72 measurements. These shorter separations were chosen such that they would still have sensitivity in the depths considered for the simulations.

The reflectance data from the Monte Carlo simulations for various anomaly locations and detector geometries is imported in to implemented Diffusion solution code in MATLAB and the reconstructed $\Delta\mu_a$ values for the region covered by the optode geometry(8cmX 6cm) are displayed as images. The $\Delta\mu_a$ are also exported to excel sheet for quantitative analysis and the 2D plots for the center of the anomaly are drawn. The quantitative analysis is done by

calculating the Full Width at Half Maximum (FWHM) for the same in MATLAB platform for different data sets.

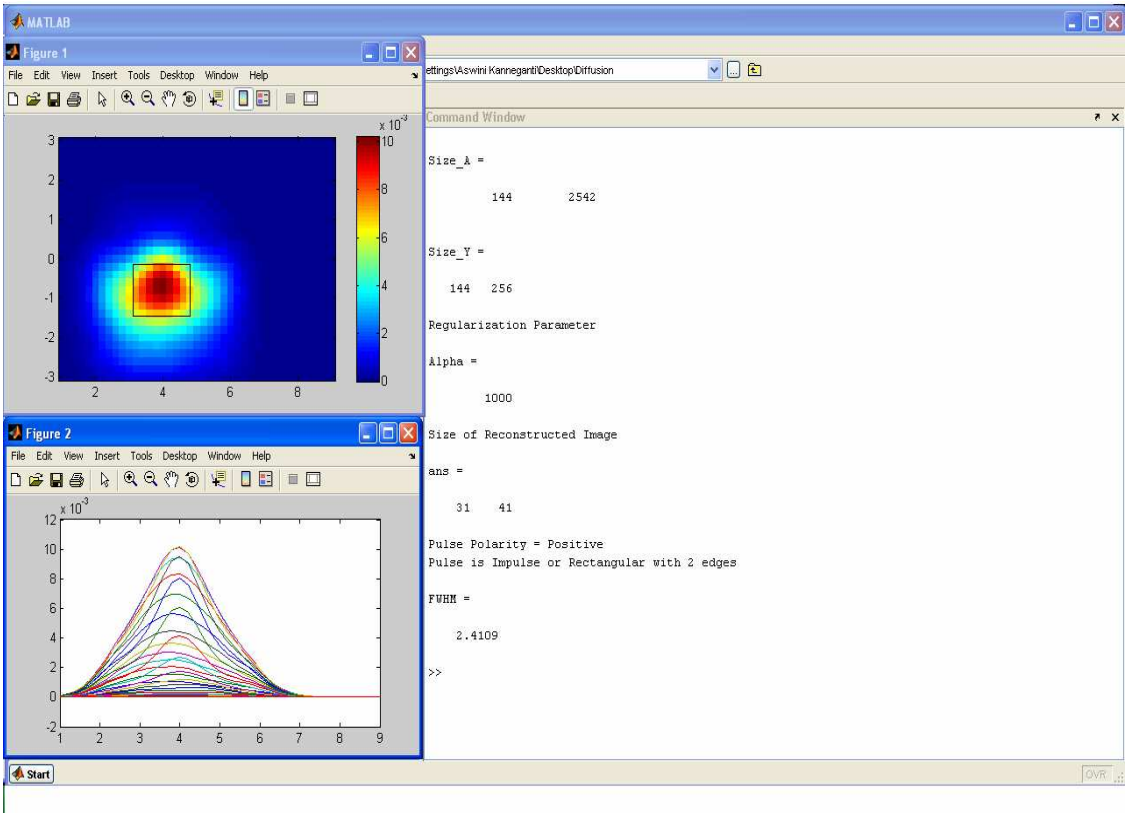

Figure-2.13: Screen shot of the MATLAB code output in MATLAB command window

The figure 2.13 is the screen shot of the command window in MATLAB after the reconstruction code is run. The screenshot shows the output image, graph and the displayed numerical results.

CHAPTER 3

RESULTS AND DISCUSSION

The cortical activation is simulated using the tMCimg Monte Carlo Transport program for the typical brain optical properties given above. The reflectance output for various activation locations and sizes of the 8 channel CW5 geometry and the 12 channel Proposed Geometries is compared.

3.1 Comparison of the performance for optode geometries with varying activation regions size

The reflectance data was generated for optode geometries by varying the size of the activation region. The simulated volume using Monte Carlo is 10cm X 10cm and the activation regions are square shaped with sides 0.6cm, 1cm and 2cm centered at (4,5). The reconstructed images are documented.

3.1.1 Anomaly 1

The reconstructed images of Anomaly 1, a 0.6cm sided square centered at (4,5cm) at a depth of 0.5-1cm for the different optode geometries are compared. The regularization parameter chosen for reconstruction is 0.1.

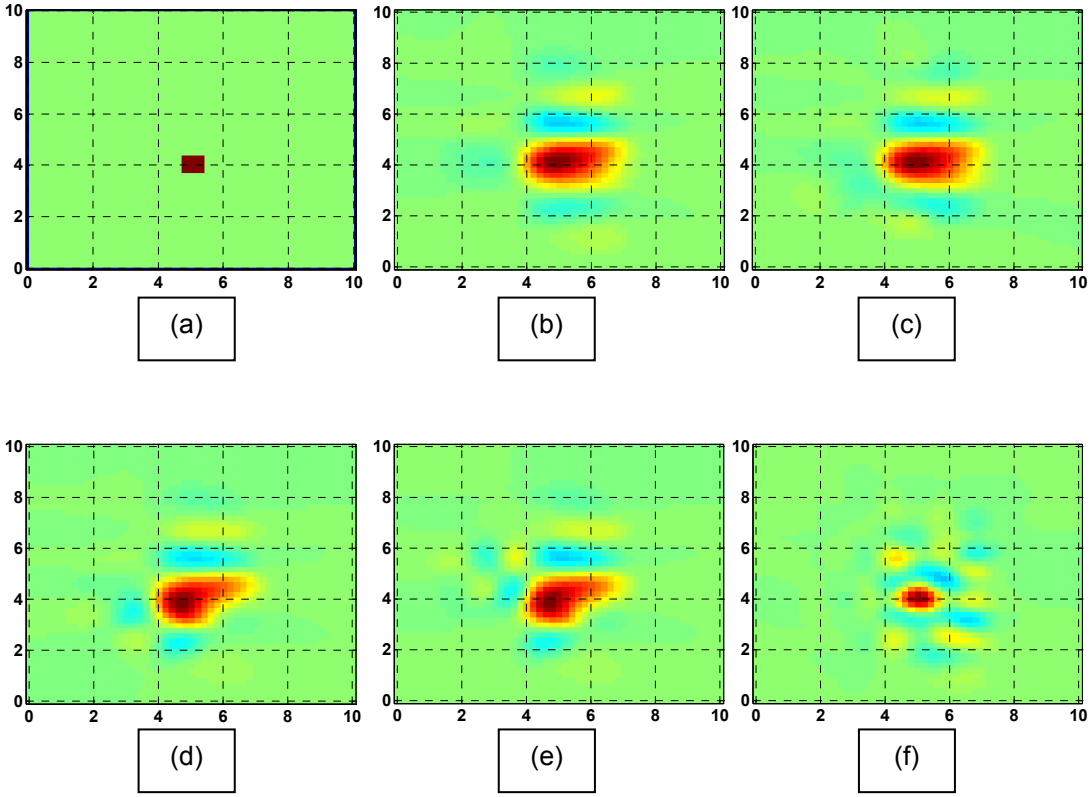

Figure-3.1: (a) True anomaly location, a square of side 0.6cm at 0.5-1cm depth and reconstructed images obtained using the optode geometries (b) 8 channel CW5 geometry, (c) Proposed Geometry I, (d) Proposed Geometry II, (e) Proposed Geometry III, (f) Proposed Geometry IV

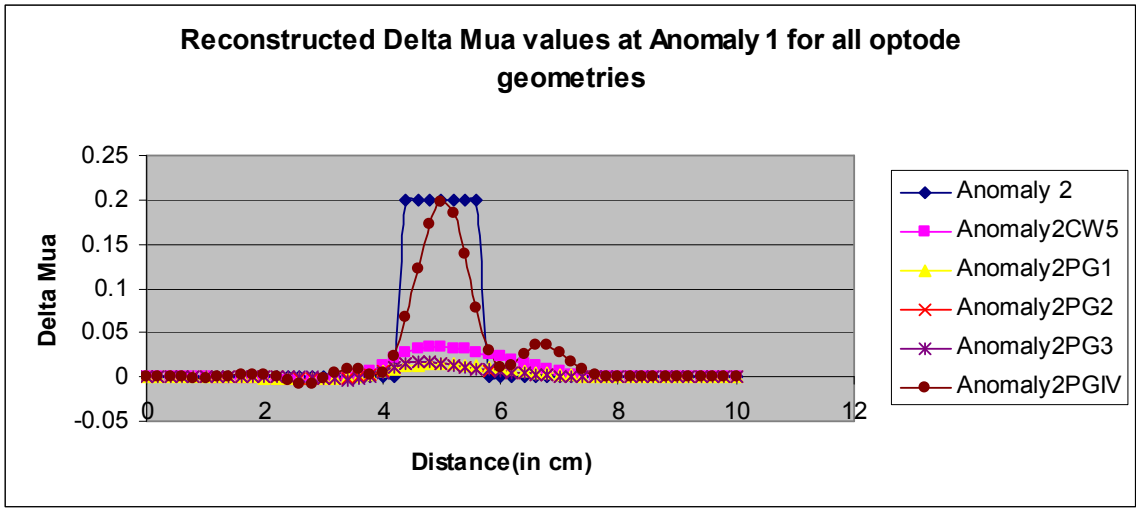

Figure-3.2: 2D Plot depicting the $\Delta\mu_a$ values for all geometries at Anomaly 1

Figure 3.1 shows the reconstructed images for anomaly 1 for CW5, PG I, PG II, PG III, and PG IV optode geometries. When the results are compared with the true location of the anomaly, it is evident that as the number of source-detector pairs is increased, the resultant reconstructed images get better. The resolution for the activation regions is also degraded. As the number of measurements increase, the optimal distance between two activation regions that can be resolved could be reduced due to improved spatial resolution. The localization has been improved by 0.2cm for the case of denser PG IV geometry. The approximate dimensions of the activation region could also be measured. Figure 3.2 shows a 2D plot of the reconstructed $\Delta\mu_a$ values for the four proposed geometries compared with the true $\Delta\mu_a$ values of the anomaly. Despite the optimal solution for the inverse problem, it is seen that PG IV geometry reconstructed $\Delta\mu a$ are relatively close to the true values when compared with those reconstructed using rest of the proposed geometries and the existing CW5 geometry.

3.1.2 Anomaly 2

The reconstructed images of Anomaly 2, a 1cm sided square centered at (4,5cm) at a depth of 0.5-1cm for the different optode geometries are compared.

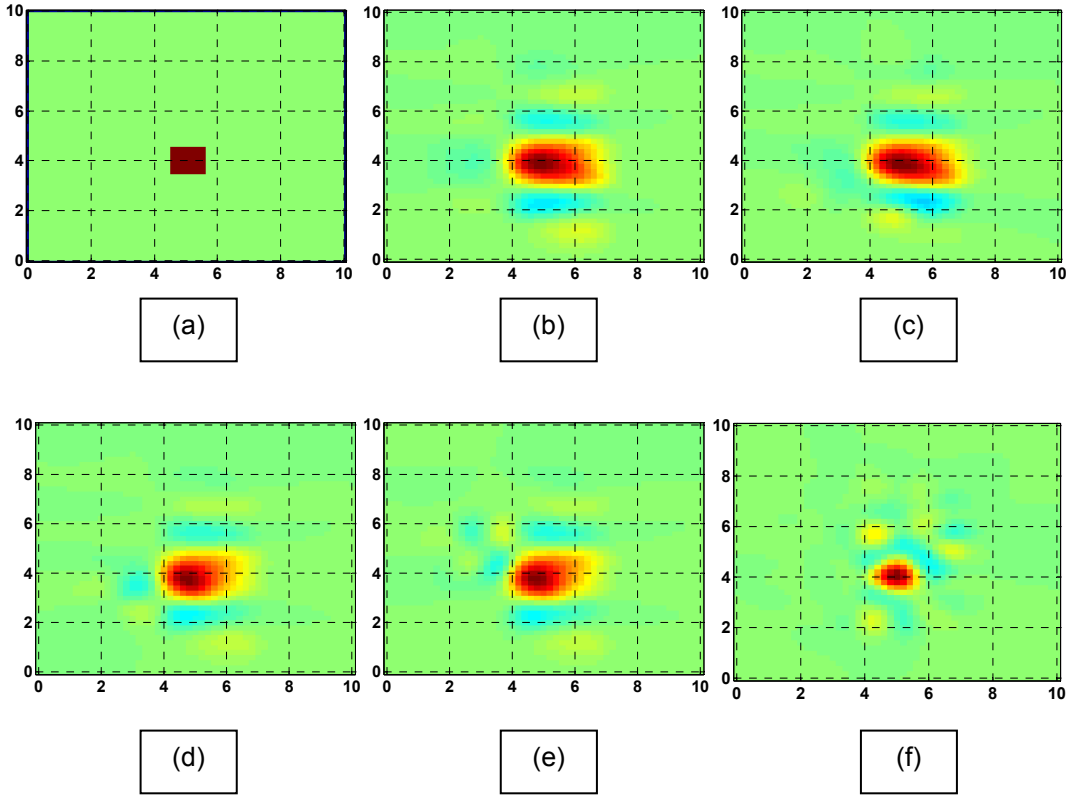

Figure-3.3: (a) True anomaly location, a square of side 1cm at depth 0.5-1cm and reconstructed images obtained using the optode geometries (b) 8 channel CW5 geometry, (c) Proposed Geometry I, (d) Proposed Geometry II, (e) Proposed Geometry III, (f) Proposed Geometry IV

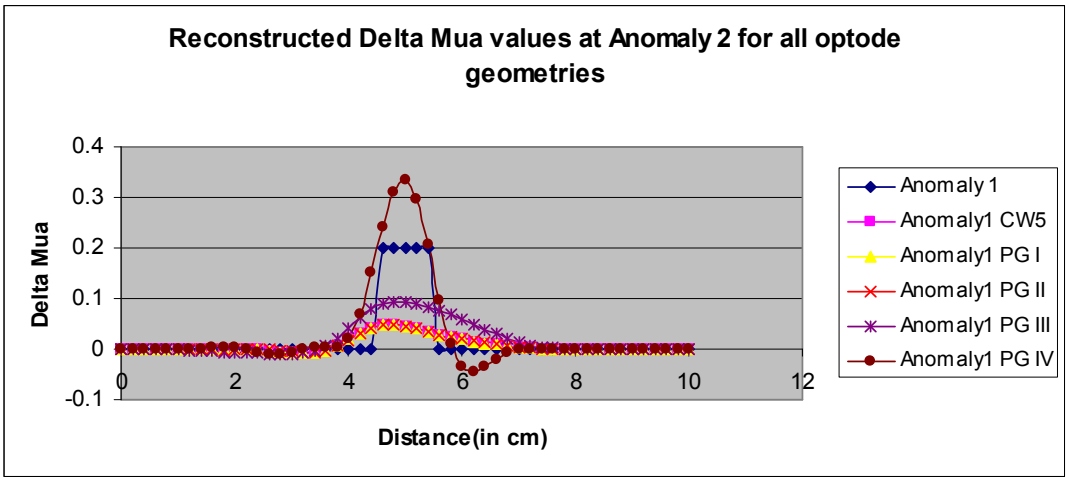

Figure-3.4: 2D Plot depicting the $\Delta\mu_a$ values for all geometries at Anomaly 2

Figure 3.3 shows the reconstructed images for anomaly 2 for CW5, PG I, PG II, PG III, and PG IV optode geometries. When the results are compared with the true location of the anomaly, it is evident that as the number of source-detector pairs is increased, the resultant reconstructed images get better. As the number of measurements increase, in the case of 12 channel PG II and PG III and denser PG IV geometry improved spatial resolution is observed in the images when compared with the images got from 8 channel CW5 geometry. 12 channel PG I geometry showed no considerable improvement and the reason could be the inclusion of the additional channels far from the activation region resulting in no effective signal detection from the activation area. A shift in the location of the center was observed for PG II and PG III and it could be accounted for the fact that unsymmetrical sampling of the imaging volume gives false activation regions. The localization of the activation region is improved by 0.2cm for the maximum detectors added PG IV geometry. Figure 3.4 shows a 2D plot of the reconstructed $\Delta\mu_a$ values for the four proposed geometries compared with the true $\Delta\mu_a$ values of the anomaly. Despite the optimal solution for the inverse problem, it is seen that PG IV geometry reconstructed $\Delta\mu a$ are relatively close to the true values followed by PG III when compared with those reconstructed using rest of the proposed geometries and the existing CW5 geometry.

3.1.3 Anomaly 3

The reconstructed images of Anomaly 3, a 2cm sided square centered at (4,5cm) at a depth of 0.5-1cm for the different optode geometries are compared.

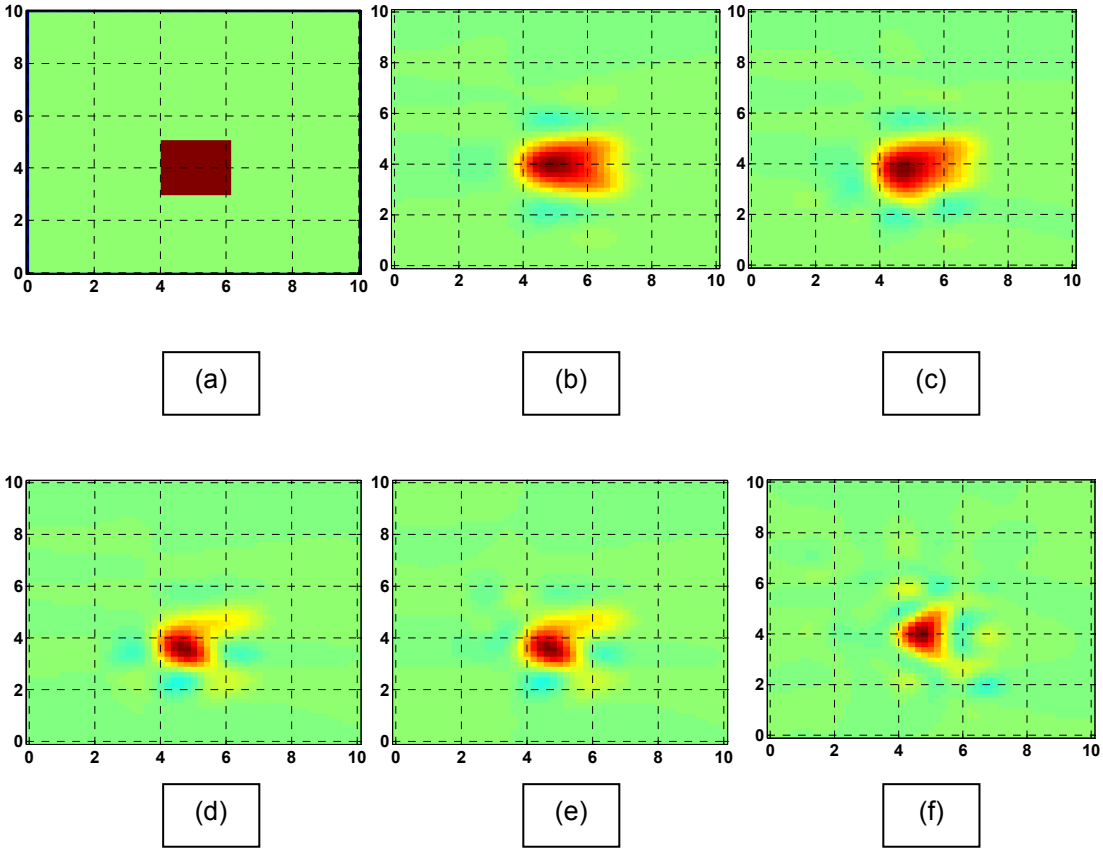

Figure- 3.5: (a) True anomaly location, a square of side 2cm at depth of 0.5-1cm and reconstructed images obtained using the optode geometries (b) 8 channel CW5 geometry, (c) Proposed Geometry I, (d) Proposed Geometry II, (e) Proposed Geometry III, (f) Proposed Geometry IV

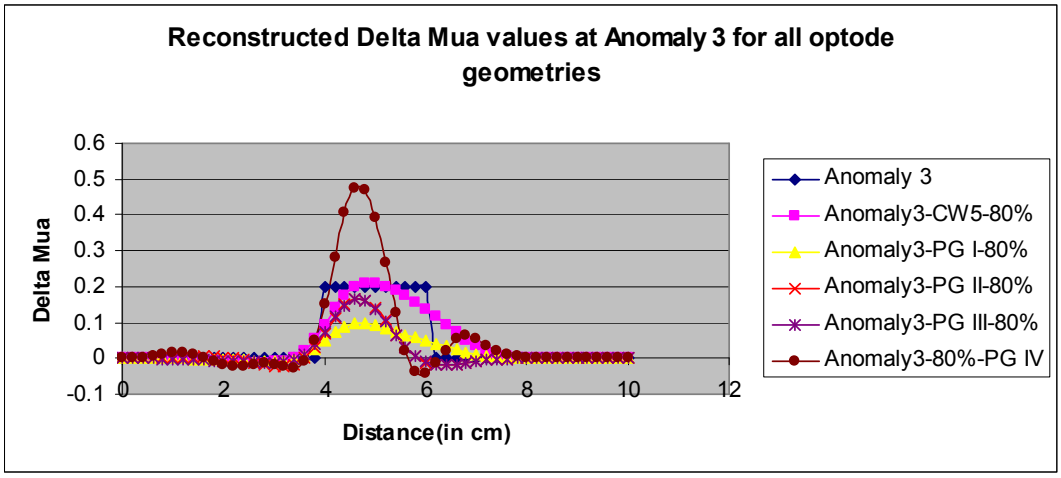

Figure-3.6: 2D Plot depicting the $\Delta\mu_a$ values for all geometries at Anomaly 3

Figure 3.5 shows the reconstructed images for anomaly 3 for CW5, PG I, PG II, PG III, and PG IV optode geometries. As the number of measurements increase, in the case of 12 channel PG II and PG III and denser PG IV geometry improved spatial resolution is observed in the images when compared with the images got from 8 channel CW5 geometry. 12 channel PG I geometry showed no considerable improvement and the reason could be the inclusion of the additional channels far from the activation region resulting in no effective signal detection from the activation area. A shift in the location of the center was observed for the proposed geometries. The culprit is the unsymmetrical sampling of the imaging volume in the case of PG I, PG II and PG III. The lateral shift observed in the case of PG IV geometry reconstructed image could be due inclusion of too many measurements and thereby averaging the signal obtained can result in false center location. Figure 3.6 shows a 2D plot of the reconstructed $\Delta\mu_a$ values for the four proposed geometries compared with the true $\Delta\mu_a$ values of the anomaly. Despite the optimal solution for the inverse problem, it is seen that PG II, PG III and CW5 geometry reconstructed Δμa are relatively close to the true values when compared with those reconstructed using rest of the proposed geometries.

3.1.4 Full Width at Half Maximum Comparison

For the quantitative comparison of the optode geometries, we calculated the Full Width at Half Maximum using the code written in the MATLAB platform.

Table-3.1 Full Width at Half Maximum (FWHM) Comparison for optode geometries for various anomaly sizes

Optode Geometry	Anomaly 1 (in cm)	Anomaly 2 (in cm)	Anomaly 3 (in cm)
8 Channel - CW5	2.2764	2.1945	2.2594
12 Channel - PG I	2.2479	2.2447	2.0261
12 Channel - PG II	1.6665	1.6873	**1.2579**
12 Channel - PG III	**1.6305**	**1.6743**	**1.2840**
Maximum Detector - PG IV	1.0115	1.0374	1.1094

Table 3.1 shows the Full Width at Half Maximum (FWHM) values calculated using a code implemented in MATLAB. On an average a marked decrease in the FWHM is found when the size of the anomaly is increased. It is also evident from the above table that the PG II and PG III has the least FWHM value compared to the existing 8 channel CW5 optode geometry for all the three anomaly locations. The FWHM corresponds to the spatial resolution of the images and hence as the FWHM decreases, there is considerable improvement in the spatial resolution. The spatial resolution has been improved by an average of ~30% in the case of 12 channel geometries PG II and PG III when compared with the existing 8 channel CW5 optode geometry. Due to asymmetrical arrangement of the detectors, PG II is chosen as the best within the limited hardware channels available. Denser geometry PG IV though not practically possible due limited number of channels in CW5 gives best results for improved spatial resolution over the existing CW5 geometry by an average of ~52% for different activation sizes.

3.2 Performance of the optode geometries for changes in the μ_a perturbation in the activation region

The activation of brain cells increases the local blood flow and thereby increases the concentration of chromophores oxy and deoxy hemoglobin which in turn effects the absorption coefficient in that region. The relative change in the absorption coefficient at each point in the imaging volume constitutes the reconstructed image. By varying the absorption coefficient

relative to the rest of the background brain, the effect of contrast in the reconstructed images could be observed. The background optical absorption coefficient is decreased by 80% and 40% for the activation regions. The resultant reconstructed images of the simulated reflectance data show a linear relationship between the true perturbation and reconstructed $\Delta\mu_a$.

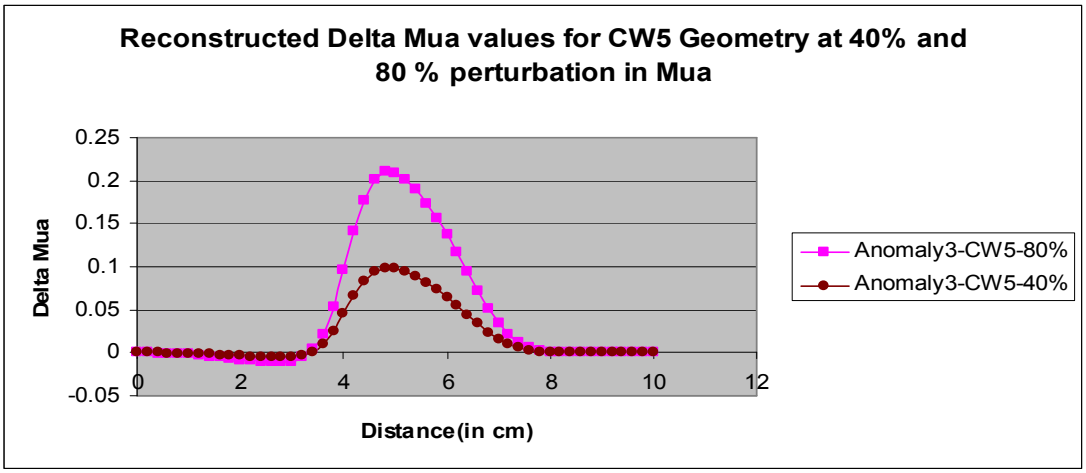

Figure-3.7: 2D plot compares 80% perturbation in μ_a to 40 % perturbation of CW5 optode geometry for Anomaly 3, a square of side 2cm at depth of 0.5-1cm

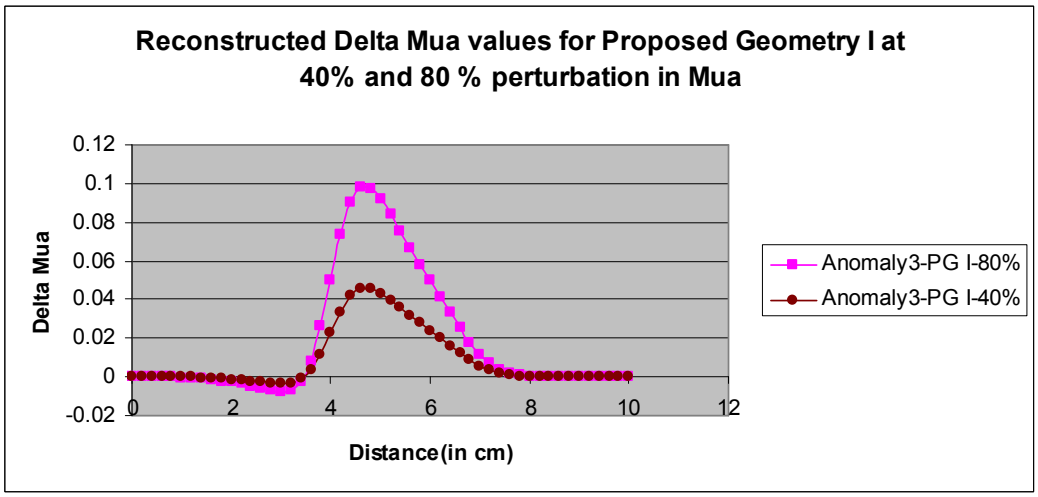

Figure-3.8: 2D plot compares 80% perturbation in μ_a to 40 % perturbation of PG I optode geometry for Anomaly 3, a square of side 2cm at depth of 0.5-1cm

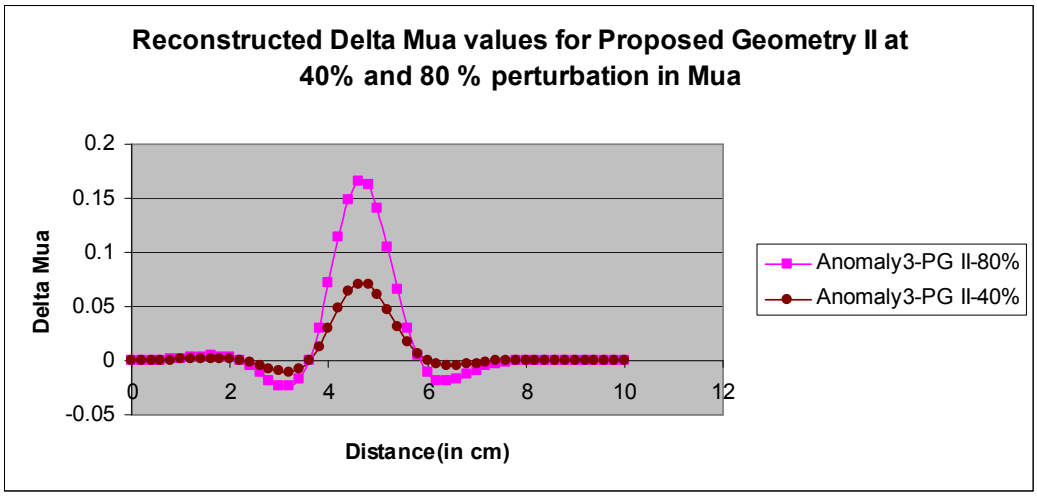

Figure-3.9: 2D plot compares 80% perturbation in μ_a to 40 % perturbation of PG II optode geometry for Anomaly 3, a square of side 2cm at depth of 0.5-1cm

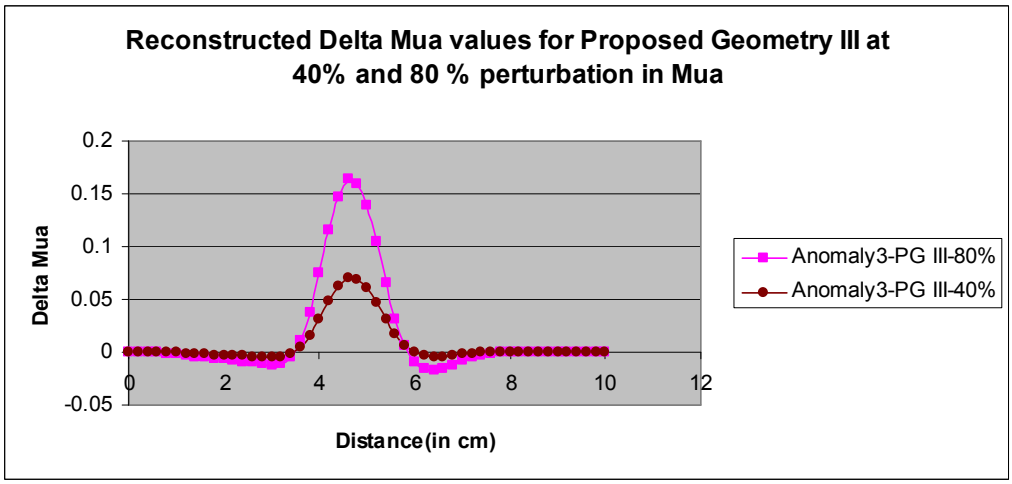

Figure-3.10: 2D plot compares 80% perturbation in μ_a to 40 % perturbation of PG III optode geometry for Anomaly 3, a square of side 2cm at depth of 0.5-1cm

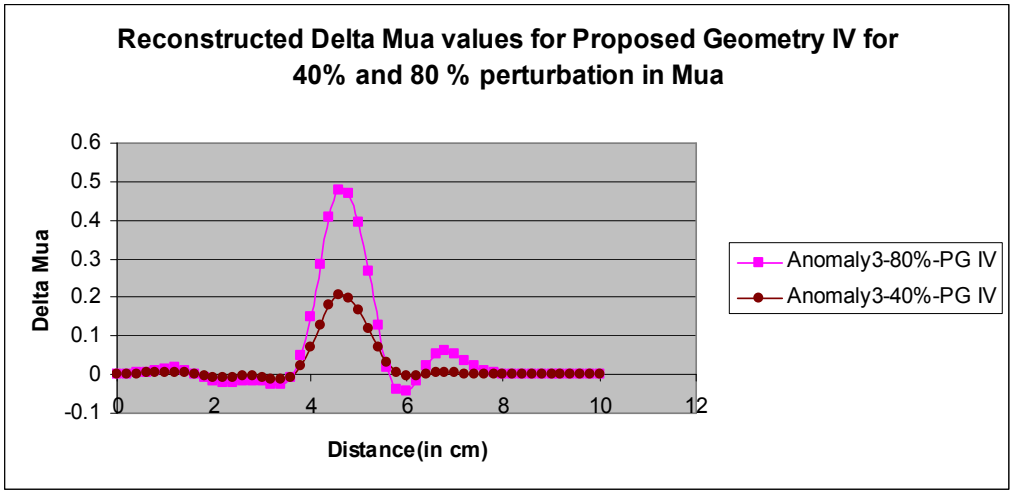

Figure-3.11: 2D plot compares 80% perturbation in μ_a to 40 % perturbation of PG IV optode geometry for Anomaly 3, a square of side 2cm at depth of 0.5-1cm

Figure 3.7 – 3.11 shows the reconstructed $\Delta\mu_a$ values for anomaly 3, a square of side 2cm at depth of 0.5-1cm with μ_a perturbed by 40% and 80% from the background absorption coefficient in the activated regions with optode geometries CW5, PG I, PG II, PG III and PG IV respectively. It is observed from the graphs that there exists a linear relationship between the μ_a perturbation and the reconstructed $\Delta\mu_a$ values.

Table-3.2 Full Width at Half Maximum (FWHM) Comparison for 40% and 80% contrast change in the activation region

Optode Geometry	40 % Perturbation in Mua	80% Perturbation in Mua
8 Channel - CW5	2.2520	2.2594
12 Channel - PG I	2.0635	2.0261
12 Channel - PG II	**1.2925**	**1.2579**
12 Channel - PG III	1.3191	1.2840
Maximum detectors - PG IV	1.1533	1.1094

Table-3.2 shows the calculated Full Width at Half Maximum for anomaly 3 at depth 0.5-1cm with μ_a perturbed by 40% and 80% from the background absorption coefficient in the activated regions with optode geometries CW5, PG I, PG II, PG III and PG IV. It is clear from the table that the relative change in the absorption coefficient in the activation region to the background properties has not influenced the spatial resolution significantly. Thus, the contrast of the activation region does not contribute much to the spatial resolution. The results are relevant for simulation data, wherein the background is not heterogeneous. In humans, the heterogeneity of the imaging tissue camouflages the actual activation region.

3.3 Comparison of performance of the proposed geometries at various depths with existing CW5 geometry

As the anomaly is placed deeper, the signal to noise ratio decreases. The anomaly of 2cm side centered at (4, 5 cm) but varied at depths of 0.5 -1cm, 1-1.5cm, 1.5 - 2cmm and 2-2.5cm.The reflectance data is used to generate the reconstructed images of the same.

3.3.1 At depth of 0.5-1cm

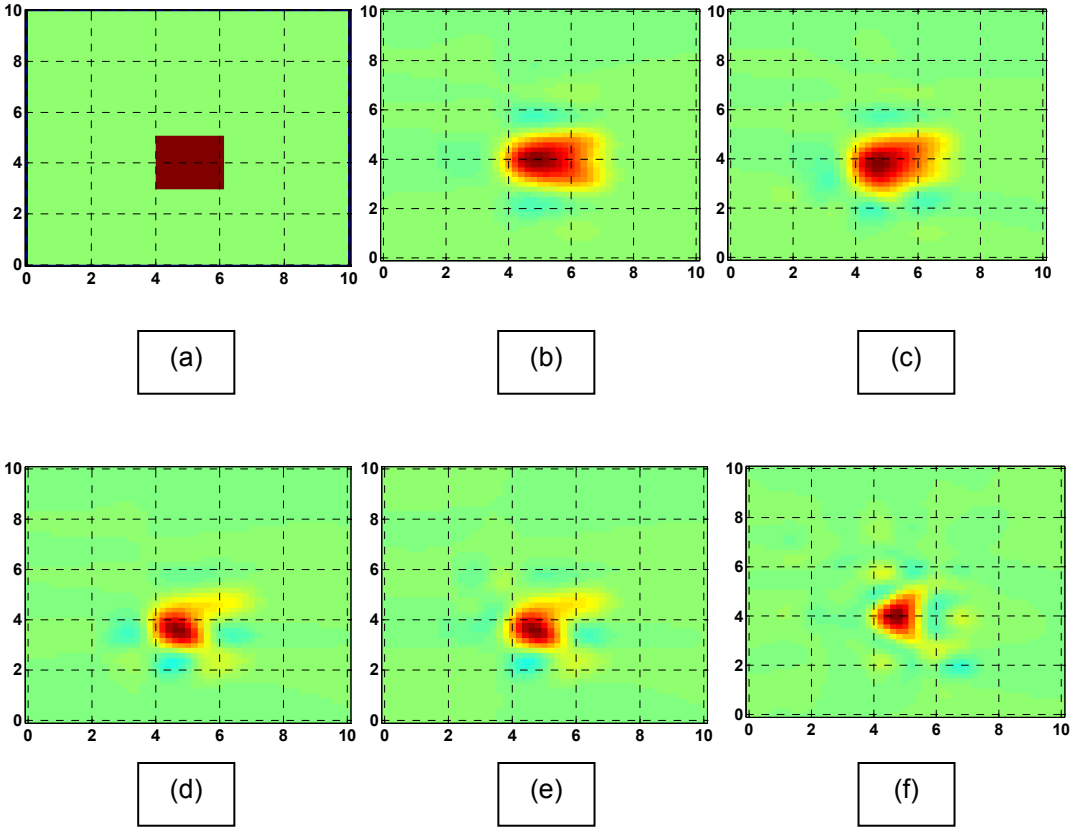

Figure-3.12: Anomaly 3, a square of side 2cm at depth of 0.5-1cm, (a) True location of the anomaly and reconstructed images obtained using the optode geometries (b) CW5 geometry, (c) Proposed Geometry I, (d) Proposed Geometry II, (e) Proposed Geometry III, (f) Proposed Geometry IV

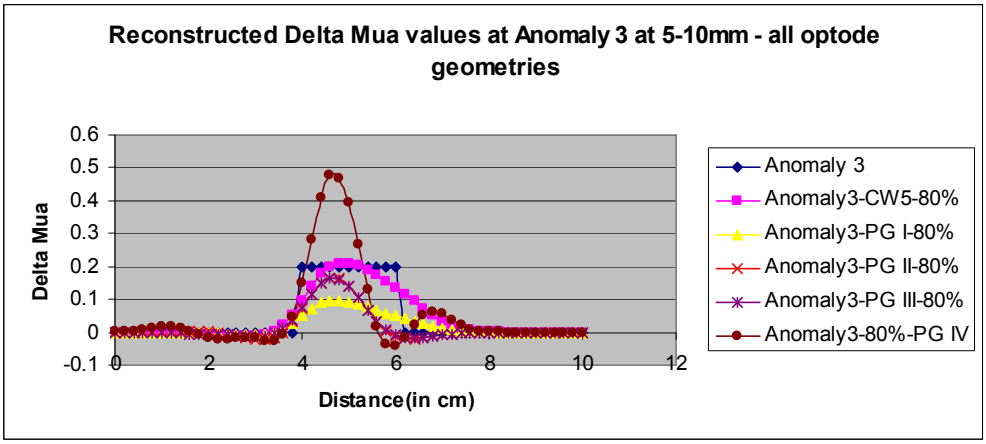

Figure-3.13: 2D plot shows the reconstructed Δμa values for all geometries, for anomaly 3, a square of side 2cm at depth of 0.5-1cm

Figure 3.12 shows the reconstructed images of 2cm side square anomaly at depth of 0.5-1 cm for various optode geometries. When the results are compared with the true location of the anomaly, it is evident that as the number of source-detector pairs is increased, the spread in the resultant reconstructed images reduces. As the number of measurements increase, improved spatial resolution is observed in the images. A shift in the location of the center was observed for the proposed geometries. The reason is the unsymmetrical sampling of the activation region by the neighboring measurements in the case of PG I, PG II and PG III. The lateral shift observed in the case of PG IV geometry reconstructed image could be due inclusion of too many measurements and thereby averaging the signal obtained can result in false center location. Figure 3.13 shows a 2D plot of the reconstructed $\Delta\mu_a$ values for the four proposed geometries compared with the true $\Delta\mu_a$ values of the anomaly. Despite the optimal solution for the inverse problem, it is seen that PG II, PG III and CW5 geometry reconstructed $\Delta\mu_a$ are relatively close to the true values when compared with those reconstructed using rest of the proposed geometries.

3.3.2 At depth of 1-1.5cm

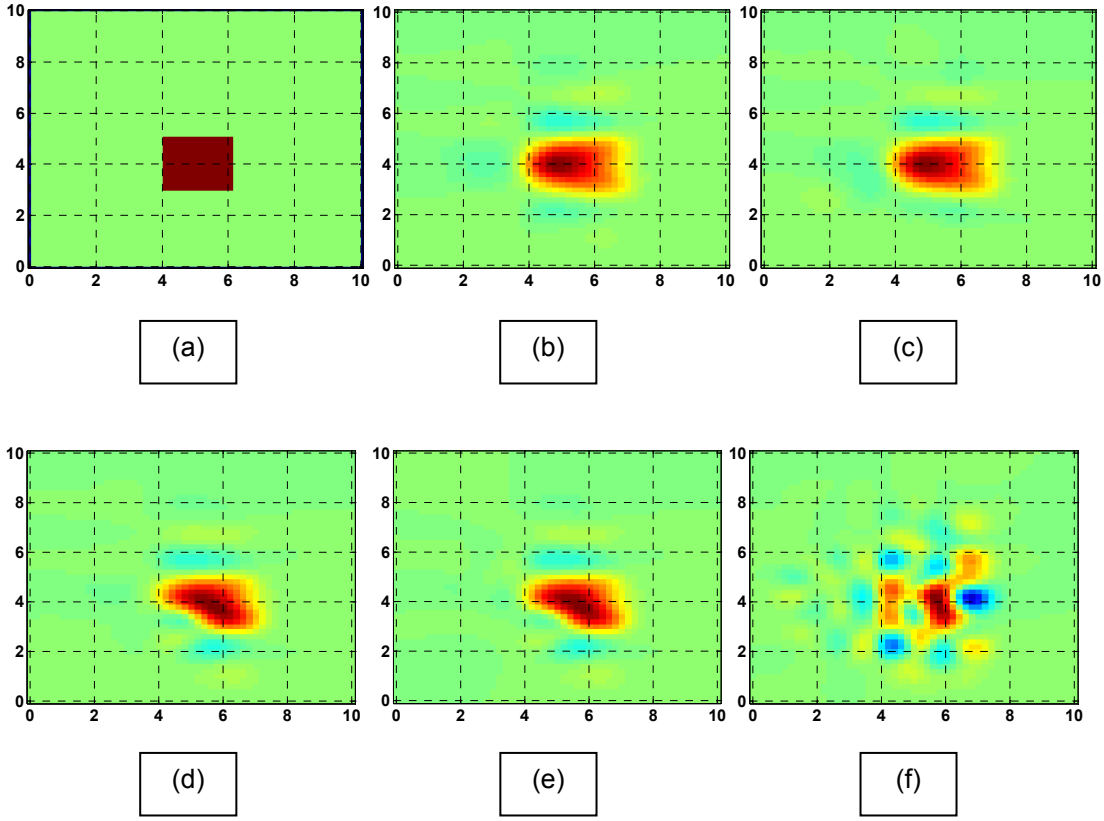

Figure-3.14: Anomaly 3, a square of side 2cm at depth of 1-1.5cm, (a) True location of the anomaly and reconstructed images obtained using the optode geometries (b) CW5 geometry, (c) Proposed Geometry I, (d) Proposed Geometry II, (e) Proposed Geometry III, (f) Proposed Geometry IV

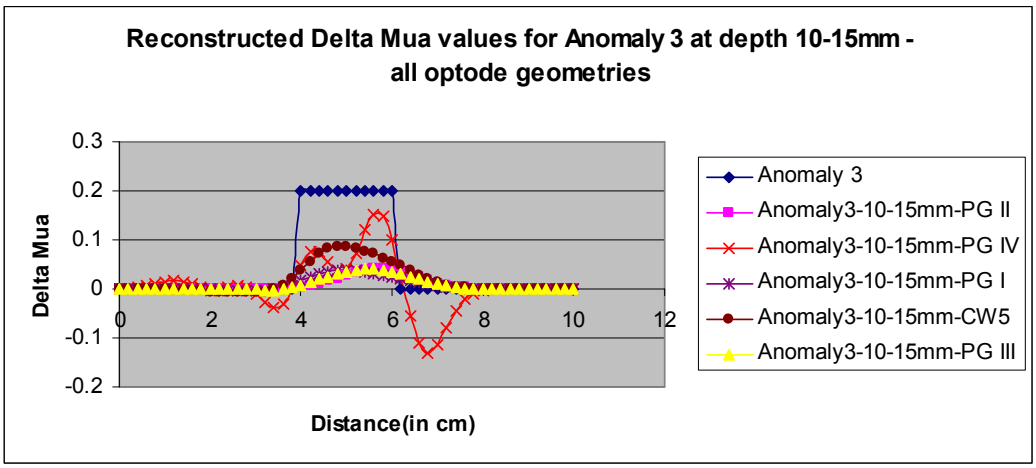

Figure-3.15: 2D plot shows the reconstructed Δμa values for all geometries, for anomaly 3, a square of side 2cm at depth of 1-1.5cm

Figure 3.14 shows the reconstructed images of 2cm side square anomaly at depth of 1-1.5 cm for various optode geometries. When the results are compared with the true location of the anomaly, it is evident that as the number of source-detector pairs is increased, the spread in the resultant reconstructed images reduces incase of the 12 channel optode geometries when compared with the 8 channel CW5 geometry. As the number of measurements increase, improved spatial resolution is observed in the images. The change in the activation region position relative to the sources and detectors affects the image performance immensely. Owing to the fact that the unsymmetrical sampling of the activation region by the neighboring measurements in the case of PG I, PG II and PG III and relatively lesser source – detector separation, the penetration depth decreases and the background noise adds up. The denser PG IV reconstructed image is inconclusive due to the significant effect of the background noise. As the number of measurements at smaller source detector separations is increased in the case of denser PG IV geometry, the effective signal from the activation region is masked by the unwanted signals measured. Figure 3.15 shows a 2D plot of the reconstructed $\Delta\mu_a$ values for the four proposed geometries compared with the true $\Delta\mu_a$ values of the anomaly. Despite the optimal solution for the inverse problem, it is seen that filtered PG IV reconstructed $\Delta\mu a$ values are relatively close to the true values followed by CW5 when compared with those reconstructed using rest of the proposed geometries.

3.3.3 At depth of 1.5-2cm

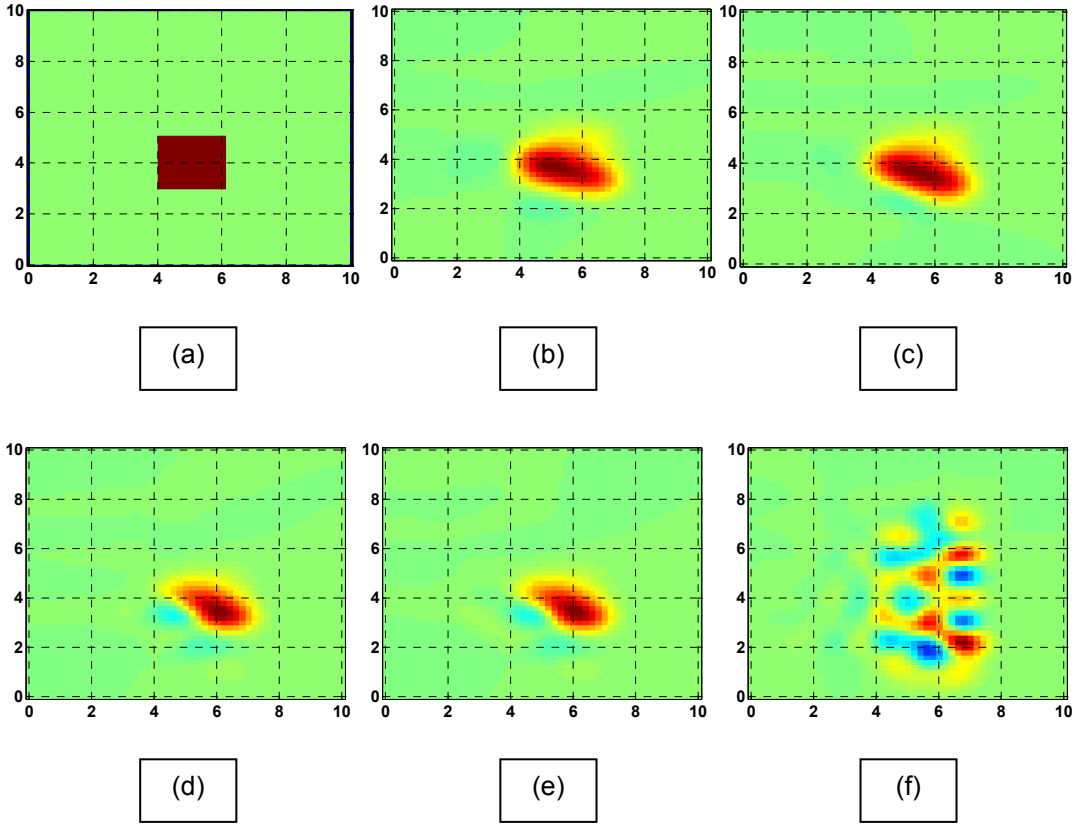

Figure-3.16: Anomaly 3, a square of side 2cm at depth of 1.5-2cm, (a) True location of the anomaly and reconstructed images obtained using the optode geometries (b) CW5 geometry, (c) Proposed Geometry I, (d) Proposed Geometry II, (e) Proposed Geometry III, (f) Proposed Geometry IV

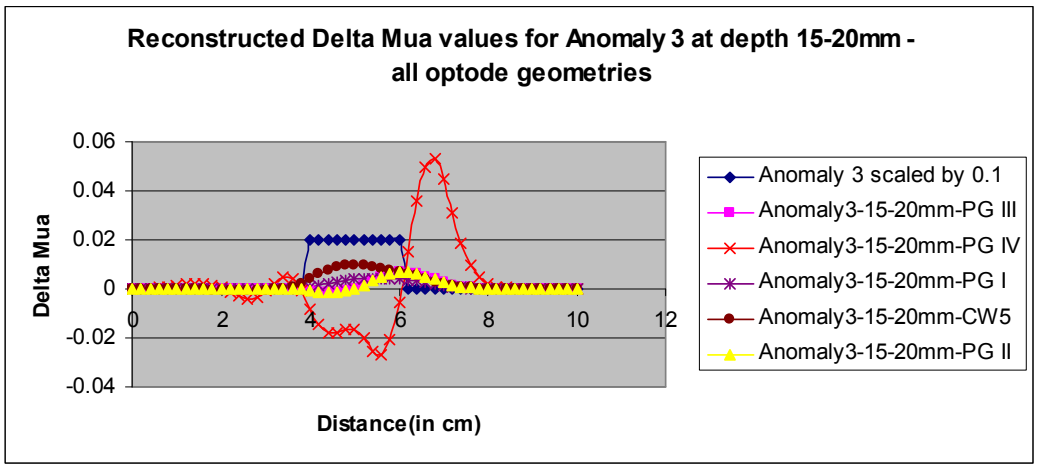

Figure-3.17: 2D plot shows the reconstructed Δμa values for all geometries, for anomaly 3, a square of side 2cm at depth of 1.5-2cm

3.3.4 At depth of 2-2.5cm

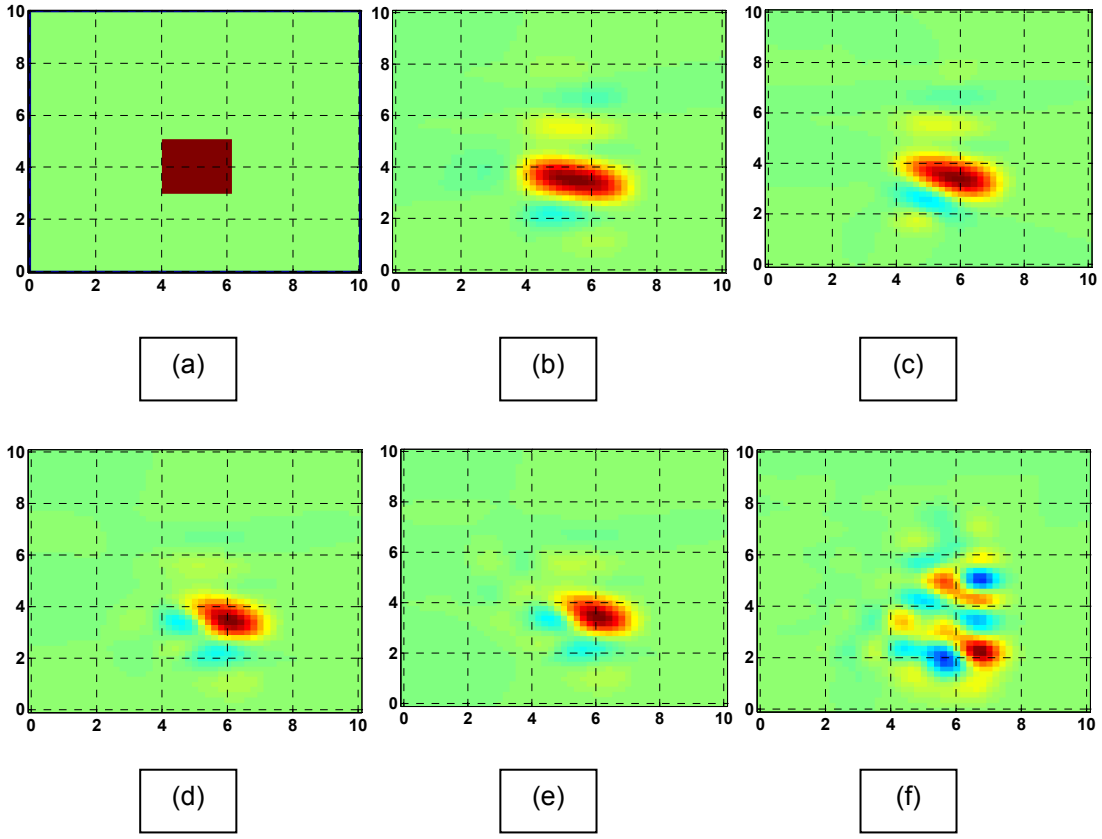

Figure-3.18: Anomaly 3, a square of side 2cm at depth of 2-2.5cm, (a) True location of the anomaly and reconstructed images obtained using the optode geometries (b) CW5 geometry, (c) Proposed Geometry I, (d) Proposed Geometry II, (e) Proposed Geometry III, (f) Proposed Geometry IV

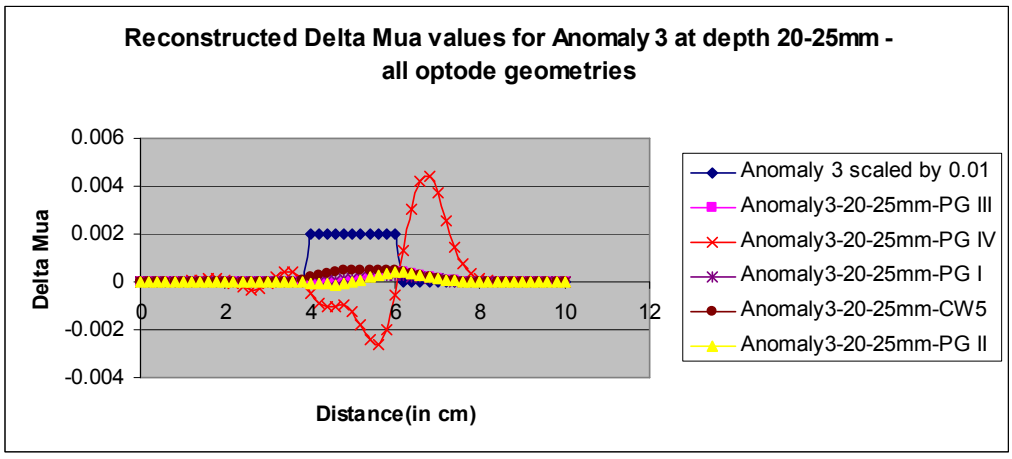

Figure-3.19: 2D plot shows the reconstructed Δμa values for all geometries, for anomaly 3, a square of side 2cm at depth of 2-2.5cm

Figure 3.16 and Figure 3.18 shows the reconstructed images for anomaly 3 at depths 1.5-2cm and 2-2.5cm for all geometries respectively. As the depth of the anomaly location increase, more noise is added to the image resulting in the distortion of the reconstructed activation region location. The location of the activation region is shifted from the true location not only in the 12 channel geometries PG I, PG II and PG III but also in the denser detector geometry PG IV. As explained earlier, the results obtained from PG IV could be termed inconclusive due to the influence of background noise. The thumb rule for penetration depth and source detector separation states that the penetration depth is half the source detector separation.[7] The minimum source detector separation for the proposed geometries is 1.5cm and the effective penetration depth is approximately 1cm and hence the proposed geometries failed for anomaly depths greater than 1.5cm.

3.3.5 Full Width at Half Maximum comparison - effects of increased depth

Table-3.3 FWHM comparison at different depths of all the geometries for anomaly 3, a square of side 2cm

Optode Geometry	**Depth 0.5-1 (in cm)**	**Depth 1-1.5 (in cm)**	**Depth 1.5-2 (in cm)**	**Depth 2-2.5 (in cm)**
8 channel - CW5	2.2594	2.2397	2.4058	2.5423
12 channel - PG I	2.0261	2.2184	2.4011	1.9862
12 channel - PG II	**1.2579**	**1.9142**	**1.4990**	**1.4855**
12 channel - PG III	1.2840	2.1475	1.5044	1.4875
Maximum detector - PG IV	1.1094	0.8469	0.9625	0.9609

Table 3.3 shows the FWHM (in cm) calculated for anomaly side of 2cm at depths of 0.5 -1cm, 1-1.5cm, 1.5-2cm and 2-2.5cm for all the geometries. It is observed that the FWHM for PG II is the least at all depths for all geometries resulting in significant enhancement in the spatial resolution. PG IV is relatively more effective in improving the spatial resolution for depths

less than 1.5cm. Though an improved spatial resolution is observed there is no effective localization of the anomaly.

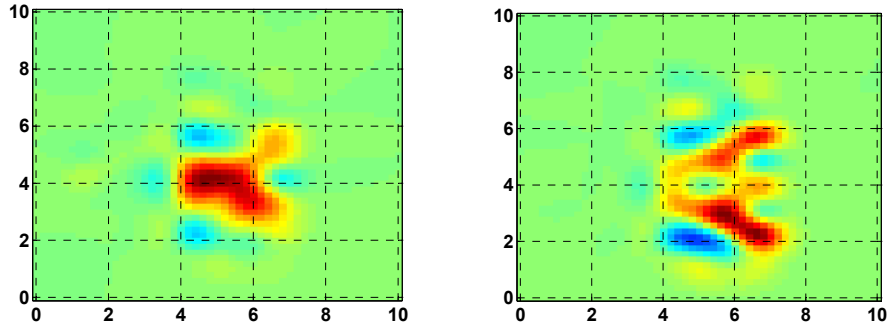

Figure-3.20: Anomaly 3, a square of side 2cm at (a) depth 1-1.5cm and (b) depth 1.5-2cm reconstructed image using the maximum detector PG IV geometry with regularization parameter $\alpha = 1$

Figure 3.20 shows the reconstructed image of anomaly 3, a square of side 2cm at depth 1-1.5cm and 1.5-2cm from the reflectance measurements done using the maximum detector geometry proposed, PG IV. The regularization parameter was changed to 1 from 0.1. The activation region images show considerable decrease in the background noise and also improved localization of the anomaly at the expense of degraded spatial resolution when compared with that of the image obtained by using regularization parameter 0.1 at depths of 1-1.5cm. For anomaly located at depth 1.5-2cm, the spatial resolution improved by just 40% and localization by 1cm when $\alpha = 1$ was used

3.4 Comparison of the performance of the optode geometries for lateral shift in the anomaly location

The activation region is moved laterally at depth of 1-1.5cm. Activation region placed directly under a source location results in ineffective localization of the anomaly and also the spatial resolution worsens. It can be improved by using denser optode geometry, which effectively increases the spatial sampling of the imaging volume.

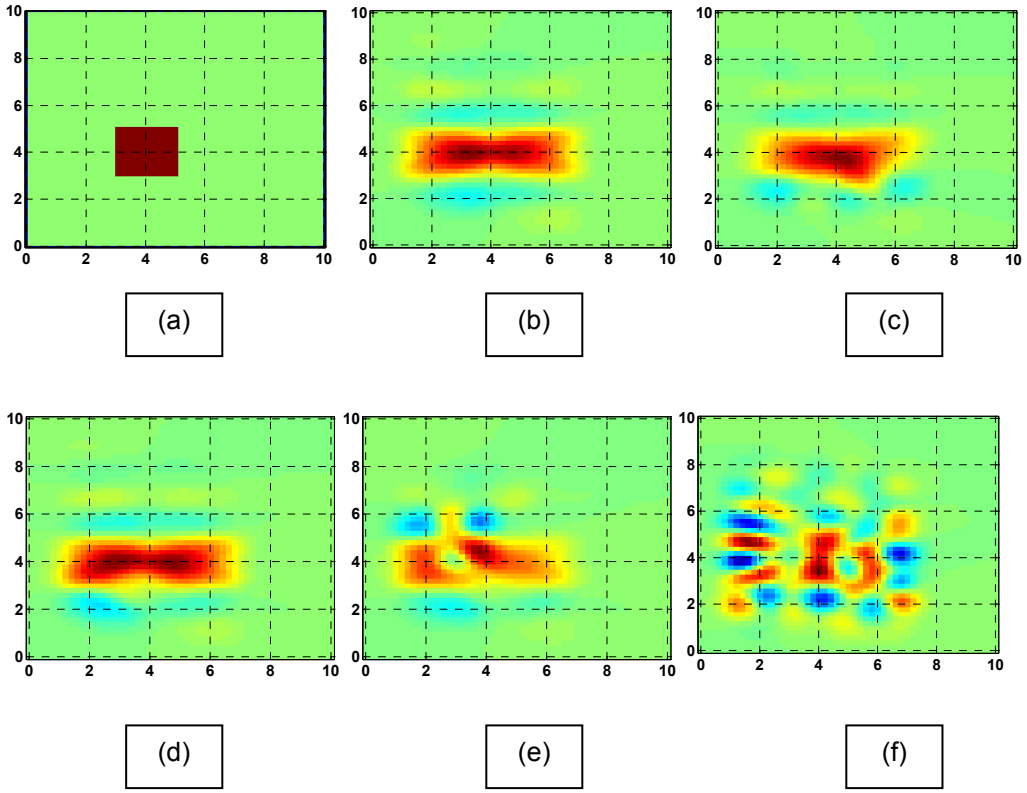

Figure-3.21: Anomaly 3, a square of side 2cm at depth 1-1.5cm centered at (4,4), (a) True location of the anomaly and reconstructed images obtained using the optode geometries (b) CW5 geometry, (c) Proposed Geometry I, (d) Proposed Geometry II, (e) Proposed Geometry III, (f) Proposed Geometry IV

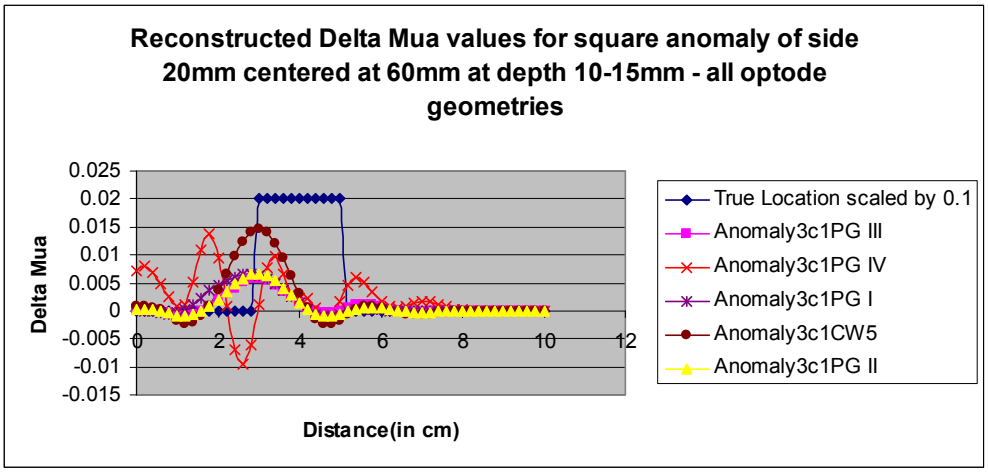

Figure-3.22: 2D plot shows the reconstructed Δμa values for all geometries, for anomaly 3, a square of side 2cm at depth 1-1.5cm centered at (4, 4)

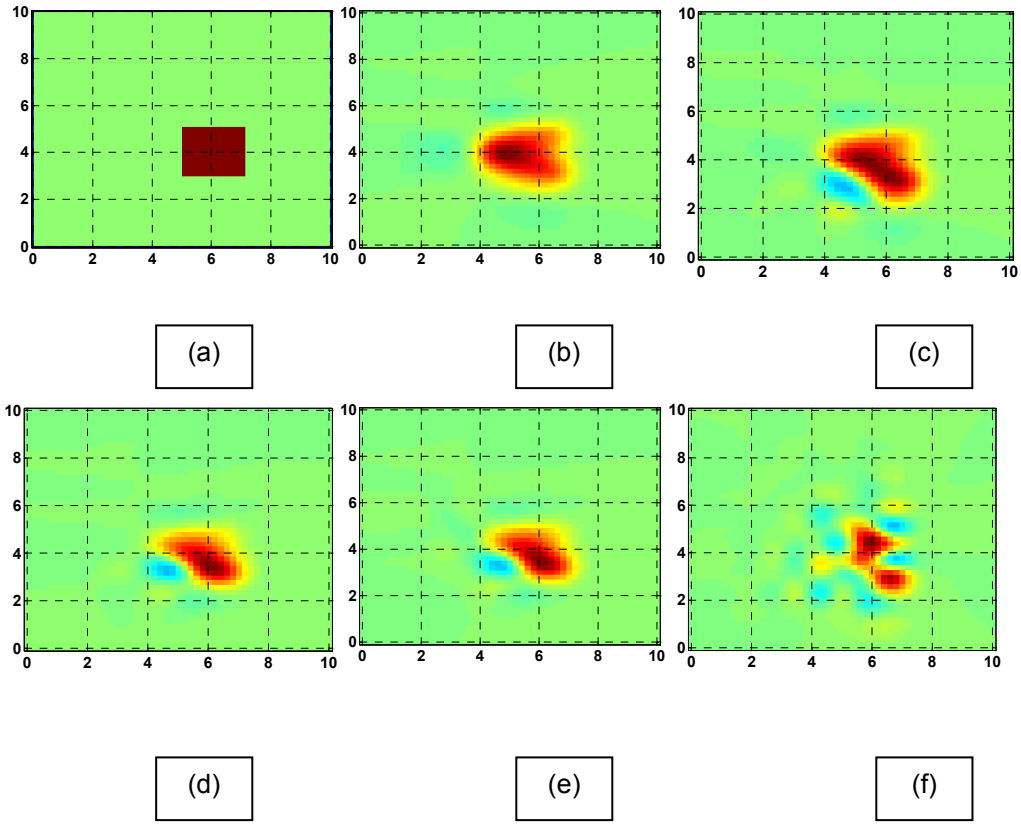

Figure-3.23: Anomaly 3, a square of side 2cm at depth 1-1.5cm centered at (6,4), (a) True location of the anomaly and reconstructed images obtained using the optode geometries (b) CW5 geometry, (c) Proposed Geometry I, (d) Proposed Geometry II, (e) Proposed Geometry III, (f) Proposed Geometry IV

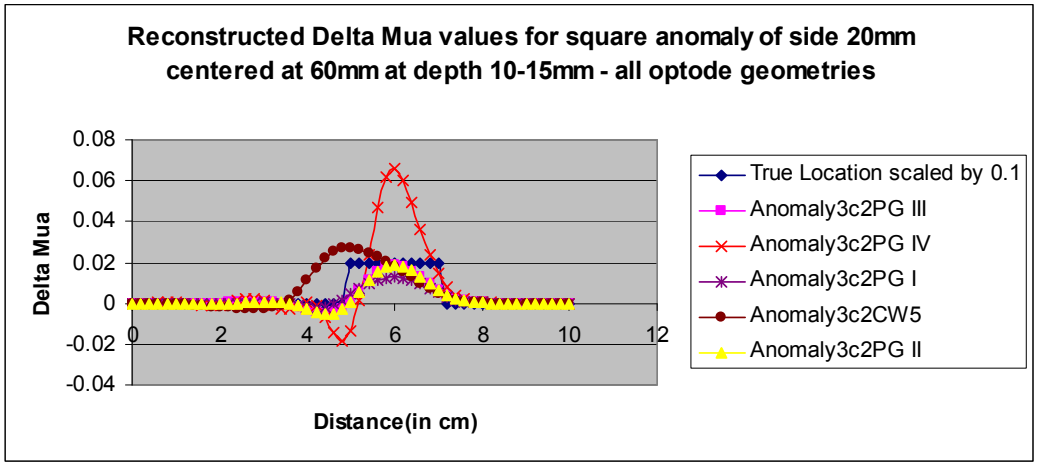

Figure-3.24: 2D plot shows the reconstructed Δμa values for all geometries, for anomaly 3, a square of side 2cm at depth 1-1.5cm centered at (6, 4)

Figure 3.21 and Figure 3.23 shows the reconstructed images for anomaly centered at (4,4cm) at depth 1-1.5cm and (4,6cm) at depth 1-1.5cm for all optode geometries respectively. The position of the anomaly was set such that it is exactly underneath the second source and third source which is considered a sweet spot because of the least measurements. All optode geometries give a totally distorted activation locations. Despite background noise, PG IV geometry gives an effective position within 0.2cm of the true location. Figure 3.22 and Figure 3.24 shows a 2D plot for the reconstructed images in figure 3.21 and figure 3.23 respectively. It is observed that the reconstructed Δμa values are considerably deviated from the original. The center of the anomaly was also shifted by a great deal.

3.5 Effect of wrongly assumed background properties during reconstruction

The optical properties of the imaging volume are often not known correctly therefore the effects of incorrectly assumed background properties in the reconstruction algorithm are analyzed.

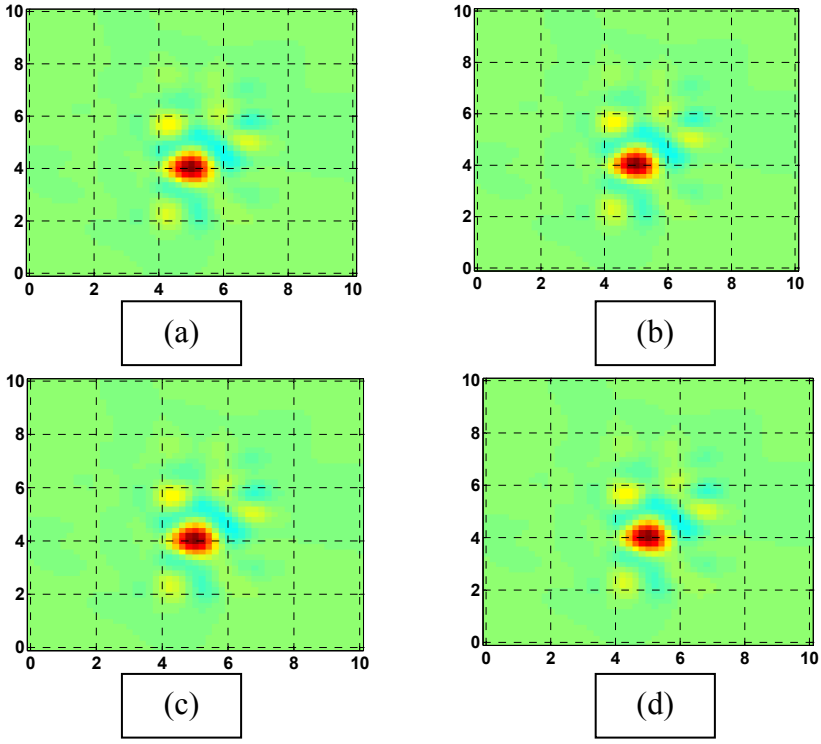

Figure-3.25: Reconstructed Anomaly 2 images for Proposed Geometry IV when, (a)Correctly assumed background properties (b)15 % off, (c) 20% Off (d) 50% off

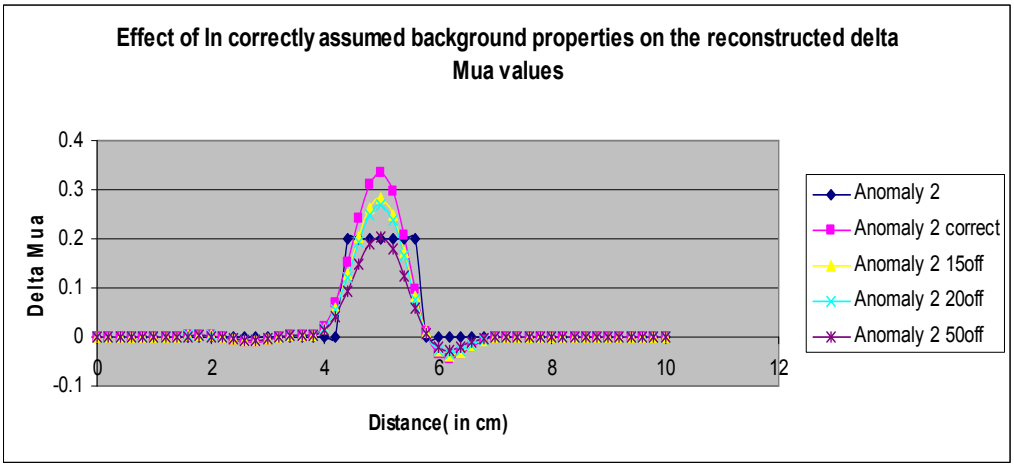

Figure-3.26: 2D plot shows the reconstructed Δμa values for Proposed Geometry IV when background optical properties are assumed incorrectly.

Table 3.4 Full Width at Half Maximum Comparison for incorrectly assumed background properties

Optode Geometry	Correct Background Properties	15 % off from true value	20 % Off from true value	50% off from true value
PG IV	1.0374	1.0345	1.0340	1.0333

Figure 3.25 shows the reconstructed images obtained for incorrectly assumed background optical properties. The optical properties were off by 15%, 20% and 50% from the typical brain optical properties. The images show no considerable difference for different error percentages. Figure 3.26 depicts a 2D graph for the optode geometries for wrongly assumed background properties. The error in the optical properties assumption effects the reconstruction quantitatively i.e., the Δμa values are deviated from the true values considerably. Table 3.3 shows the FWHM calculated for the same and it is evident that the reconstruction algorithm is robust in the case of spatial resolution but fails quantitatively.

CHAPTER 4

CONCLUSION AND FUTURE WORK

The objective of the work done was to improve the spatial resolution of the cortical activation maps for different activation region sizes, locations, contrast and of errors in the assumed background optical properties while employing the highest practically possible detector spatial sampling that can be attained with our CW5 system. Due to the limited number of channels available in that system, namely 24, one can only utilize 12 detectors per brain hemisphere. Results from optode geometries using the maximum possible number of detectors (PG I, PG II, PG III) as well as results from a denser geometry (PG IV), only feasible by a different optical imaging system (DYNOT [25]), are compared to the performance of a 4-source 8-detector arrangement that our group has been using up to date.

It was found that image spatial resolution depends on the position of the activation region relative to the source-detector positions. For anomaly of sizes 0.6cm and 1cm located at a depth of 0.5-1cm, the 12-channel PG II and PG III geometries yielded approximately 30 % improvement in spatial resolution when compared to the existing 8 channel CW5 optode arrangement. The higher density PG IV geometry yielded an improvement of ~55%. For a square anomaly of 2 cm side at a depth of 0.5-1cm, the 12-channel PG II and PG III geometries yielded ~43% and PG IV ~50% improvement in the spatial resolution whereas no considerable improvement in spatial resolution was observed for the 12 channel PG I geometry. The localization of the anomaly was moved to the true location by 0.2 cm when the densest PG IV detector was used, but no notable change was observed for the 12-channel geometries compared to the 8-channel one.

As the location of the activation region with side of 2 cm was moved deeper inside the imaging volume to 1-1.5cm, 15-2cm and 2-2.5cm, it was observed that the spatial resolution improved at the expense of ineffective localization of the anomaly location. For anomaly at 1.5-

2cm, typical depth for the activations in the brain, the spatial resolution is improved by 37% for 12 channel PG II geometry. It was noticed for the denser geometry PG IV, the images obtained were affected with too much background signal rendering them unreliable.

When the location of the anomaly at depths of 1-1.5cm was moved laterally such that its center lies just below a source location, considered as a blind spot the location of the activation region was moved within 0.2cm of the true location for maximum detector PG IV geometry. The 8 channel CW5 geometry generated activation maps show a deviation in the location of the anomaly by 1.2cm from its true location. The 12-channel optode arrangements when compared with the existing 8-channel CW5 optode geometry showed no considerable improvement in anomaly localization though a slight improvement in spatial resolution was observed when 12 channel PG II was used.

We also noticed that when the absorption coefficient was decreased by 80 % as well as 40 % below its baseline value, the results show a linear relationship between the perturbed optical property values and the reconstructed ones. The FWHM comparison showed no significant change and thus the contrast does not affect the spatial resolution of the reconstruction notably. However, this result is only relevant to the above simulated data. In an experimental measurement on humans, the reconstructed baseline optical property map typically exhibits high spatial heterogeneity and therefore lower contrast by an activation region may cause that region to be masked by the background fluctuations.

It was also found that incorrectly assumed background optical properties for the reconstruction do not affect spatial resolution drastically as seen from the quantitative FWHM comparisons performed. Though the reconstructed $\Delta\mu a$ values were affected, the algorithm was robust to changes in spatial resolution.

In précis, we have proposed an improved optode geometry that includes the currently unused 4 channels of our CW5 system, increasing the total number of detectors per hemisphere from 8 to 12, to enhance the spatial resolution with which cortical activation regions

are reconstructed by approximately 35%. We have found that the spatial resolution of an activation region is influenced by its size and location relative to the optode geometry. Due the limitation in the number of channels available resulting in the asymmetric sampling of the imaging volume by adding just four more detectors, the localization of the anomaly was moved by 0.4cm for 8 channel CW5 geometry and 0.9cm for 12 channel PG II geometry from the true location for anomaly at depth of 1.5-2cm. The image reconstruction algorithm based on the diffusion solution was robust to the changes in spatial resolution. A salient finding of this work was that if it were possible to add more detectors than CW5 could accommodate, spatial resolution and localization may not have improved beyond a certain point for anomaly depths of 1.5-2.5 cm. A potential culprit for this problem is that that large number of detectors at short source-detector separations contributes reflectance signal from photons that have traveled superficially and above the true anomaly location. Therefore these measurements are likely to have contributed more to increased noise versus enhancing detection of the activation signal. Our future work goals are two-fold: (1) To optimize the relative number of detectors at short source-detector separations (1.5 cm) to enhance the relative contribution of more distant detectors that probe deeper tissues and therefore carry a larger proportion of signal from regions where activation occurs in order to maximize spatial resolution, (2) Implement a layered brain tissue model for the A-matrix, so that the blurring effect of spatially heterogeneous optical properties is taken into account more accurately. We will validate the practical success of our two future goals by performing appropriate experiments on two-layer tissue simulating phantoms and on humans.

APPENDIX A

DIFFUSION SOLUTION CODE IN MATLAB

```
%%%%%%%%%%%%%%%%%%%%%%%%%%%%%%%%%%%%%%%%%%%%%%%

%%%%%%%%%%%%%%%%%%%%%%%%%%%%

% Diffusion Solution discussed in D.A Boas_NI_2004

% Image Reconstruction---Inverse Problem

%%%%%%%%%%%%%%%%%%%%%%%%%%%%%%%%%%%%%%%%%%%%%%%

%%%%%%%%%%%%%%%%%%%%%%%%%%%%


% All Lengths in cm.

% Voxel Size is cm

clear all

% The optical properties of the medium

Musp=10.5;

Mua=0.25;

% Musp=12.075;  % 15%

% Mua=0.2875; % 15%

% Musp=12.6;  % 20%

% Mua=0.3;    %20%

% Musp=15.75;

% Mua=0.375;

% The Source Matrix

SrcPos = [ 4 2 0
           4 4 0
           4 6 0
           4 8 0 ];
 % The Detector Matrix

 DetPos = [ 1 1 0
            1 2 0
            1 3 0
            1 4 0
            1 5 0
            1 6 0
```

```
        1 7 0
        1 8 0
        1 9 0
        2.5 1 0
        2.5 2 0
        2.5 3 0
        2.5 4 0
        2.5 5 0
        2.5 6 0
        2.5 7 0
        2.5 8 0
        2.5 9 0
        5.5 1 0
        5.5 2 0
        5.5 3 0
        5.5 4 0
        5.5 5 0
        5.5 6 0
        5.5 7 0
        5.5 8 0
        5.5 9 0
        7 1 0
        7 2 0
        7 3 0
        7 4 0
        7 5 0
        7 6 0
        7 7 0
        7 8 0
        7 9 0];

   Det_Size = size(DetPos);

 % Source - Detector Pairing

% [ Src Det Freq]

 SD = [ 1 1 1
      1 2 1
      1 3 1
      1 4 1
      1 10 1
      1 11 1
      1 12 1
      1 13 1
      1 19 1
      1 20 1
      1 21 1
      1 22 1
      1 28 1
      1 29 1
      1 30 1
```

1 31 1
2 2 1
2 3 1
2 4 1
2 5 1
2 6 1
2 11 1
2 12 1
2 13 1
2 14 1
2 15 1
2 20 1
2 21 1
2 22 1
2 23 1
2 24 1
2 29 1
2 30 1
2 31 1
2 32 1
2 33 1
3 4 1
3 5 1
3 6 1
3 7 1
3 8 1
3 13 1
3 14 1
3 15 1
3 16 1
3 17 1
3 22 1
3 23 1
3 24 1
3 25 1
3 26 1
3 31 1
3 32 1
3 33 1
3 34 1
3 35 1
4 6 1
4 7 1
4 8 1
4 9 1
4 15 1
4 16 1
4 17 1
4 18 1
4 24 1
4 25 1
4 26 1

```
    4 27 1
    4 33 1
    4 34 1
    4 35 1
    4 36 1];

   SD_Size = size(SD);

 % Same Src Det patring can be written for second frequency with the

% third coloumn as 2 stating it's for the second frequency.

% In case of additonal frequencies, the Mua and Musp would also be

% matrices witj index refering to the frequency index.

 % Speed of light

 V = 2.1898e+08;

  % Reff represents the fraction of photons that is internally diffusely

% reflected at the boundary.

 Reff = 0.4684;

 % Extrapolated Boundary Calculated

 zBnd = 2/3 * (1+Reff)/(1-Reff)/Musp;

 %% Compute complex wavevectors and diffusion coefficients

 D = V./(3*Musp);

 % Forward

%where f index of frequency

%    K(f,:) = sqrt(V .* Muao ./ D ...

%        - i * (2*pi * (Freq) * 1e6)) ./ D)

%    % Adjoint

%    Kr(f,:)= sqrt(V .* Muao ./ D ...

%        + i * (2*pi * (Freq) * 1e6)) ./ D)

% Actual Calculation of wave vector is defined above but in this program,

% the output value from HoMer is taken. Here it is for the phantom
```

```
% measurements.
% CAUTION: This value varies from experiment to experiment.
K = 1.7321;
 % Define the thickness of the slab. Though not used for critical
% calculations in the code, it's useful for further development.
% For this phantom image reconstruction, i have taken the HoMer output
% value for the same.
 Thickness = 10;
 % Creating the Computational Volume or the image size or the reconstructed
% area definition.
% CAUTION: This value varies from experiment to experiment.
 dy = [0:0.2:10];
dx = [0:0.2:10];
dz=1;
volVoxel = 0.2 * 0.2 * 1;
%[x y z] = meshgrid( dx dy dz );
[x y z]=meshgrid(dx,dy,dz);
x = x(:);
y = y(:);
z = z(:);
nPts = length(x);
Vox = [x y z];
nMeas = size(SD,1); % Number of measurements
 % Looping over each SD Pair
 for imeas = 1:nMeas
    iSrc = SD(imeas, 1);  % Actual index
```

```
iDet = SD(imeas, 2);
iFrq = SD(imeas, 3);
Src = SrcPos(iSrc,:); % Row indicated with all the coloumns
Det = DetPos(iDet,:);
% Increased Absoption, makes the fluence go down
dmus = D/V; % used when calculating Mus
dmua = -1;
% Move Source and Detector one scattering length into the medium.
% All complex cases possible as dealt in HoMer are not considered
% here.
Src(3) = Src(3) + 1/Musp;
Det(3) = Det(3) + 1/Musp;
Img = Src;
  if (Thickness > 0)
     Img(3) = getImageCharge(Src(3), -zBnd);
  else
     Img(3) = getImageCharge(Src(3),  zBnd);
  end
%%
%%  Compute the incident response at the detector.
%%  Rescale using amplitude factors from SD structure.
PhiSrc = FD_GF(Src, Det, D, K, V);
PhiImg = FD_GF(Img, Det, D, K, V);
% Convert from photon density (J/cm^3) to fluence (W/cm^2) too
Phi0(imeas) = V * (PhiSrc - PhiImg);
Phi0(imeas) = Phi0(imeas) * 1 * 1 ;
```

```
    % Calculation for Mua only
    phiSa = slabA(Src, Vox, D, K, V, Thickness, zBnd);
    phiDa = slabA(Det, Vox, D, K, V, Thickness, zBnd);
     % A Matrix Calculation
      Atmp(1 : nPts, 1) = phiSa .* conj(phiDa) * dmua;
      % Rescale column by Source and Detector amplitudes and the volume of
    %the voxel.
      A(imeas, :) = volVoxel * 1* 1 * Atmp.' ;  % Amplitudes are not taken here but
    %can be added.
 end
 %disp(A)
%size(A)
A = A ./ (Phi0' * ones(1,size(A,2)));
 % The same matrix is being replicated for the second wavelength just for
% simplicity. But A can be calculated for specific wavelength with specific
% frequency properties.
A = [A zeros(size(A)); zeros(size(A)) A];
%size(A);
% Reconstruction
% CW5 data from HoMer. It corresponds to the Y Matrix for reconstruction
% Y from MCP can be used too.
Size_A = size(A)
Y = xlsread('HomerOrigaddA');
%Y=Y';
%figure, imagesc(Y)
Size_Y = size(Y)
```

```
% Inverse problem Reconstruction

%%%%%%%%%%%%%%%%%%%%%%%%%%%%%%%%%%%%%%%%%%%%%%%

%%%%%%%%%%%%%%%%%%%%%%%%%%%%

% Smax=max(diag(A*A'));

% I=ones(size(A*A'));

% Alpha=10^-3;

%%%%%%%%%%%%%%%%%%%%%%%%%%%%%%%%%%%%%%%%%%%%%%%

%%%%%%%%%%%%%%%%%%%%%%%%%%%%

% Regularized Inversion

a =0.1;

AtA = A'*A;

I = eye(size(A,1),size(A,1));

C = a* max(diag(AtA))*I;

R= eye( size(A,2), size(A,2));

B = A* ( R*A');

foo = R*A'*inv(B+C);

disp('Regularization Parameter')

Alpha = a

% Back Projection

%foo = A';


Ainv = full(foo);

Img = -1*Ainv*Y;

% size(Img)

%%%%%%%%%%%%%% L Curve %%%%%%%%%%%%%%%%%%%%%%%%%%%

% YRecon =A*Img;
```

```
% Error = (YRecon-Y);
% ModX = normest(Img)
% ModErr = normest(Error)
% ModY = normest(Y)
% RelErr = ModX/ModY
% GCV = (ModErr^2)/((trace(I-K*K'))^2)
% %size(Error)
%%%%%%%%%%%%%%%%%%%%%%%%%%%%%%%%%%%%%%%%%%%%%%%
%%%%%%%%%%%%%%%
% figure, imagesc(Img);
% imgt3 = Img(1:end,100:1000);
% imgt4 = imgt3(1:441);
% imgt5 = reshape(imgt4,21,21);
% figure, imagesc(imgt5);
%%%%%%%%%%%%%%%%%%%%%%%%%%%%%%%%%%%%%%%%%%%%%%%
%%%%%%%%%%%%%%%
%%%%%%%%%%%%%%%%%%%%%%%%%%%%%%%%%%%%%%%%%%%%%%%
%%%%%%%%%%%%%%%
 Image =Img;
 Image2 = reshape( Image, [length(dy) length(dx) length(dz) 2 size(Image,2)] );
 Image2=permute(Image2,[1 2 3 5 4]);
 I1min = min(min(min( min(Image2(:,:,:,:,1)) )));
 I2min = min(min(min( max(Image2(:,:,:,:,2)) )));
 I1max = max(max(max( max(Image2(:,:,:,:,1)) )));
 I2max = max(max(max( max(Image2(:,:,:,:,2)) )));
 Imin = min([I1min I2min]);
```

```
  Imax = max([I1max I2max]);
  Imin = min([Imin -Imax]);
  Imax = max([Imax -Imin]);
  Image3=mean(Image2(:,:,1,:,1),4);
  figure, imagesc( dx,dy,Image3, [Imin Imax] );
  axis xy
  %axis image
  grid on
  %figure,plot(dy,max(Image3));
  [max,ind]=max2d(Image3);
   FWHM = fwhm3(dx,Image3(ind(1), 1:end))
 % FWHM = fwhm3(dx,Image(1:end,21))
%%%%%%%%%%%%%%%%%%%%%%%%%%%%%%%%%%%%%%%%%%%%%%%
%%%%%%%%%%%%%%%%%%%%%%%%%%%%%%%%%%%%%%%%%%%%%%%
%   fid = fopen('plotdata2\ReconImageOrigadd.bin','wb');
%   fwrite(fid, Image3, 'double');
%   fclose(fid);
%Outline of Activation ROI
% bw=edge(imgt5);
% newimg=imoverlay(imgt5,bw,[0 2 0]);
% figure, imagesc(newimg)
%%%%%%%%%%%%%%%%%%%%%%%%%%%%%%%%%%%%%%%%%%%%%%%
%%%%%%%%%%%%%%%%%%%
% Import the resulatnt Δμa values to excel
% figure,plot(Image3(1:end,1:end,1));
% figure, plot(Image3(20,1:end));
```

```
xlswrite('plotdata2\Recon_HomerOrigaddcorrA',Image3(ind(1),1:end));

%fid = fopen('newd1.bin', 'wb')

% fwrite(fid, imgt5)
```

APPENDIX B

FULL WIDTH AT HALF MAXIMUM CODE

```
function width = fwhm3(x,y)
 % function width = fwhm(x,y)
%
% Full-Width at Half-Maximum (FWHM) of the waveform y(x)
% and its polarity.
% The FWHM result in 'width' will be in units of 'x'
%
%
% Rev 1.2, April 2006 (Patrick Egan)
 y = y / max(y);
N = length(y);
lev50 = 0.5;
if y(1) < lev50                 % find index of center (max or min) of pulse
    [garbage,centerindex]=max(y);
    Pol = +1;
    disp('Pulse Polarity = Positive');
else
    [garbage,centerindex]=min(y);
    Pol = -1;
    disp('Pulse Polarity = Negative');
end
i = 2;
while sign(y(i)-lev50) == sign(y(i-1)-lev50)
    i = i+1;
end                                 %first crossing is between v(i-1) & v(i)
interp = (lev50-y(i-1)) / (y(i)-y(i-1));
```

```
tlead = x(i-1) + interp*(x(i)-x(i-1));
i = centerindex+1;                  %start search for next crossing at center
while ((sign(y(i)-lev50) == sign(y(i-1)-lev50)) & (i <= N-1))
   i = i+1;
end
if i ~= N
   Ptype = 1;
   disp('Pulse is Impulse or Rectangular with 2 edges')
   interp = (lev50-y(i-1)) / (y(i)-y(i-1));
   ttrail = x(i-1) + interp*(x(i)-x(i-1));
   width = ttrail - tlead;
else
   Ptype = 2;
   disp('Step-Like Pulse, no second edge')
   ttrail = NaN;
   width = NaN;
end
```

REFERENCES

[1] http://www.nmr.mgh.harvard.edu/PMI/

[2] http://www.physics.upenn.edu/yodhlab/research_BO.html#spectroscopy

[3] A. Corlu, R. Choe, T. Durduran, K. Lee, M. Schweiger, S. R. Arridge, E. M. C. Hillman, and A. G. Yodh, "Diffuse optical tomography with spectral constraints and wavelength optimization," Appl. Opt. **44**, 2082-2093 (2005)

[4] A. P. Gibson, J. C. Hebden, and S. R. Arridge, "Recent advances in diffuse optical imaging," Phys. Med. Biol. 50, R1-R43 (2005).

[5] A. Kienle and M. S. Patterson, "Improved solutions of the steady-state and the time-resolved diffusion equations for reflectance from a semi-infinite turbid medium," J. Opt. Soc. Am. A **14**, 246-254 (1997)

[6] D. A. Boas, A. M. Dale, and M. A. Franceschini, "Diffuse optical imaging of brain activation: approaches to optimizing image sensitivity, resolution, and accuracy," NeuroImage 23, 275-288 (2004).

[7] CW5 instrument user manual.

[8] CW5 software user manual.

[9] T. J. Huppert, M. A. Franceschini, and D. A. Boas, “Homer: a graphical functional NIRS analysis,” Presented at 11th Annual Meeting of the OHBM, Toronto, Ontario, Canada, June 12–16, 2005, Paper 767.

[10] S. A. Prahl, M. Keijzer, S. L. Jacques, and A. J. Welch, “A Monte Carlo model of light propagation in tissue,” in SPIE Proceedings of Dosimetry of Laser Radiation in Medicine and Biology, G.J.Müller and D.H.Sliney, eds., Institute Series 5 (SPIE Press, 1989), pp. 102-111.

[11] T. Tarvainen, M. Vauhkonen, V. Kolehmainen, and J. P. Kaipio, "Coupled Radiative Transfer Equation and Diffusion Approximation," in *Photon Migration and Diffuse-Light Imaging*

II, K. Licha and R. Cubeddu, eds., Vol. SPIE Volume 5859 of Progress In Biomedical Optics And Imaging (Optical Society of America, 2005), paper TuH41.

[12] R. F. Bonner, R. Nossal, S. Havlin, and G. H. Weiss, "Model for photon migration in turbid biological media," J. Opt. Soc. Am. A **4**, 423-432 (1987)

[13] R. C. Haskell, L. O. Svaasand, T. Tsay, T. Feng, M. S. McAdams, and B. J. Tromberg, "Boundary conditions for the diffusion equation in radiative transfer," J. Opt. Soc. Am. A **11**, 2727-2741 (1994)

[14] Kienle, A., Patterson, M.S., 1997b. Improved solutions of the steady-state and the time-resolved diffusion equations for reflectance from semiinfinite turbid medium. J. Opt. Soc. Am. 14, 246–254.

[15] J. P. Culver*, V. Ntziachristos*, M. J. Holboke, and A. G. Yodh, "Optimization of optode arrangements for diffuse optical tomography: A singular-value analysis," Opt. Lett. **26**, 701-703 (2001)

[16] H. Koizumi, T. Yamamoto, A. Maki, Y. Yamashita, H. Sato, H. Kawaguchi, and N. Ichikawa, "Optical Topography: Practical Problems and New Applications," Appl. Opt. **42**, 3054-3062 (2003)

[17] S. R. Arridge, M. Cope, and D. T. Delpy, "The theoretical basis for the determination of optical pathlength in tissue: temporal and frequency analysis," Phys. Med. Biol. 37, 1531–1560 (1992).

[18] D. T. Delpy, M. Cope, P. van der Zee, S. Arridge, S. Wray, and J. Wyatt, "Estimation of optical pathlength through tissue from direct time of flight measurements," Phys. Med. Biol. 33, 1422–1442 (1988).

[19] M. Cope and D. T. Delpy, "A system for long term measurement of cerebral blood and tissue oxygenation in newborn infants by near infrared transillumination," Med. Biol. Eng. Comput. 26, 289–294 (1988).

[20] S. R. Arridge, “Optical tomography in medical imaging,” Inverse Probl. 15, R42–R93 (1999).

[21] P. C. Hansen, 'The l-curve and its use in the numerical treatment of inverse problems,' in Computational Inverse Problems in Electrocardiology (WIT Press, Southampton, 2001), pp. 119-142.

[22] D. Boas, J. Culver, J. Stott, and A. Dunn, "Three dimensional Monte Carlo code for photon migration through complex heterogeneous media including the adult human head," Opt. Express **10**, 159-170 (2002)

[23] Q. Zhao, L. J. Ji, and T. Z. Jiang, "Improving performance of reflectance diffuse optical imaging using a multicentered mode," J. Biomed. Opt. 11, 0640191-0640198 (2006).

[24] D. A. Boas, K. Chen, D. Grebert, and M. A. Franceschini, "Improving the diffuse optical imaging spatial resolution of the cerebral hemodynamic response to brain activation in humans," Opt. Lett. **29**, 1506-1508 (2004).

[25] C. Schmitz, H. L. Graber, R. L. Barbour, J. M. Lasker, and A. H. Hielscher, " A real-time system for dynamic optical tomography," in *Biomedical Topical Meeting*, (Optical Society of America, 2002), paper SuE3.

[26] E. Granot, A. Lev, Z. Kotler, B. G. Sfez, and H. Taitelbaum, "Detection of inhomogeneities with ultrasound tagging of light," J. Opt. Soc. Am. A **18**, 1962-1967 (2001).

[27] H. Koizumi, T. Yamamoto, A. Maki, Y. Yamashita, H. Sato, H. Kawaguchi, and N. Ichikawa, "Optical Topography: Practical Problems and New Applications," Appl. Opt. **42**, 3054-3062 (2003).

BIOGRAPHICAL INFORMATION

Aswini Kanneganti received her bachelor's degree in Biomedical Instrumentation engineering from Avinashilingam Deemed University, Coimbatore, India in 2006. She then pursued master's degree in Bioengineering at University of Texas at Arlington. Her research interests included medical imaging and Diffuse Optical Imaging. She will be pursuing her Doctoral research at University of Texas at Arlington.